

COPPER IODIDE AND COPPER (I) OXIDE BASED HOLE TRANSPORT
MATERIALS FOR METHYLAMMONIUM LEAD IODIDE PHOTOVOLTAIC
DEVICE OPTIMIZATION

by

Kevin Lyon, B.S.

A thesis submitted to the Graduate Council of
Texas State University in partial fulfillment
of the requirements for the degree of
Master of Science
with a Major in Physics
May 2019

Committee Members:

Alexander Zakhidov, Chair

Edwin Piner

Mark Wistey

COPYRIGHT

by

Kevin Lyon

2019

FAIR USE AND AUTHOR'S PERMISSION STATEMENT

Fair Use

This work is protected by the Copyright Laws of the United States (Public Law 94-553, section 107). Consistent with fair use as defined in the Copyright Laws, brief quotations from this material are allowed with proper acknowledgement. Use of this material for financial gain without the author's express written permission is not allowed.

Duplication Permission

As the copyright holder of this work I, Kevin Lyon, authorize duplication of this work, in whole or in part for educational or scholarly purposes only.

DEDICATION

To my wife, daughter, and son, who inspire me everyday to be a better version of myself.

ACKNOWLEDGEMENTS

I would first like to thank Dr. Alexander Zakhidov for offering much guidance and opportunity over the last two years during my work on this project. None of this would have been possible without him. I would also like to thank the other members of my committee, Dr. Edwin Piner and Dr. Mark Wistey, for being a part of my mater's degree experience here at Texas State University. Dr. Craig Swartz has also been a great help in editing my written thesis and offering his insight into my research. Additionally, I would like to thank Dr. Casey Smith and the entire staff of the Analysis Research Service Center for making materials science research possible at this university.

I would also like to thank specific members of my research group who were invaluable resources for sample processing and analysis, without whom I could not have finished this thesis on time. I would like to personally thank Dr. Chris Manspeaker for being my direct mentor for many months for all forms of laboratory processes and procedures, especially those critical to making working solar cells. Another personal thanks goes out to Mehedhi Hasan who helped me tremendously with characterization in this work, but also whose previous research gave my own project a stable foundation.

Finally, I would like to thank all my family and friends who have supported me in this endeavor. Especially, I would like to thank my wife, mother, and father for constantly giving me support and enthusiasm in my pursuits for higher education. Their continued belief in me has given my life and work purpose and direction.

TABLE OF CONTENTS

	Page
ACKNOWLEDGEMENTS	v
LIST OF TABLES	viii
LIST OF EQUATIONS	ix
LIST OF FIGURES	xi
LIST OF ABBREVIATIONS	xiv
ABSTRACT	xviii
CHAPTER	
I. INTRODUCTION	1
A Brief History of Photovoltaic Technology	1
Cost, Performance, and Practicality of Modern Solar Cells	3
Physical Principles of Operation for an Ideal Photodiode	6
Introduction to Perovskites and Application to Photovoltaics	15
CH ₃ NH ₃ PbI ₃ Crystal Structure and Useful Properties	18
II. ORGANIC PEROVSKITE PHOTOVOLTAICS	20
Anatomy of an Organic Perovskite Photovoltaic Cell	20
Practical and Theoretical Limits of Organic Perovskite Solar Cells	23
In Pursuit of Better Hole Transport Layer	27
III. DEVICE FABRICATION	34
Device Architecture	34
Device Fabrication Process	35
IV. HTL MATERIAL CHARACTERIZATION	39

Atomic Force Microscopy	39
Stylus Profilometry.....	42
Scanning Electron Microscopy	45
Energy Dispersive X-Ray Spectroscopy	48
Ultraviolet-Visible Spectroscopy	51
X-Ray Diffraction Crystallography	55
Spectroscopic Ellipsometry	58
V. DEVICE ELECTRICAL CHARACTERIZATION	67
Champion Device J-V Characterization.....	67
Device Batch Averages and Deviations for Performance Metrics	70
J-V Modeling for Finding Resistances and Ideality Factor	73
VI. CONCLUSIONS	79
Properties of Copper Iodide and Copper Oxide HTLs.....	79
Efficacy of Cu-based HTLs in Organic Perovskite Solar Cells	80
Consequences of Single Parameter Modeling of Ideality Factor	82
Considerations for Further Research	84
APPENDIX SECTION	86
REFERENCES.....	89

LIST OF TABLES

	Page
1) The hole mobilities and band gaps of PEDOT:PSS, CuI, Cu ₂ O, and CuO	31
2) B-spline modeling parameters for Cu-based HTLs deposited on glass/ITO substrates.....	63
3) Thickness predictions for ITO and HTL layers calculated from SE models with MSE values to show goodness of fit.....	65
4) Device performance metrics averages and deviations for solar cell sample populations with CuI and Cu ₂ O HTLs.....	70
5) Device J-V curve metrics averages and deviations for solar cell sample populations with CuI and Cu ₂ O HTLs	74
6) Recombination mechanisms and associated ideality factor values	82

LIST OF EQUATIONS

	Page
1) Poisson Equation for a Shockley diode	9
2) p -type minority carrier diffusion equation (differential form).....	10
3) p -type minority carrier diffusion equation (solution)	10
4) Hole and electron minority carrier currents	11
5) Total diode current equation	11
6) The Diode Law.....	11
7) Photovoltaic current equations.....	13
8) The Goldschmidt Rule.....	16
9) Fill factor equation.....	24
10) Power conversion efficiency equation.....	24
11) CuI to Cu ₂ O via NaOH dip chemical conversion equation	35
12) Complex reflectance ratio equation.....	59
13) Cauchy equation modeling refractive index as a function of wavelength.....	61
14) Mean square error equation	61
15) Ellipsometry measurement vector N equation.....	61
16) Ellipsometry measurement vector C equation.....	61
17) Ellipsometry measurement vector S equation.....	61
18) Ohmic approximation of $J(V)$ near J_{sc}	73

19) Differential resistance approximation of dV/dJ near V_{OC}	74
20) Heterojunction diffusion current equation.....	83

LIST OF FIGURES

	Page
1) The world's first solar array, invented by Charles Fritts in 1884.....	2
2) NREL Solar Cell Technology Efficiency Chart.....	5
3) Schematic diagram of an ideal $p-n$ junction diode illustrating the parameters of the depletion approximation	8
4) J-V curve of a solar cell in darkness (dotted curve) and under illumination (solid curve).....	13
5) Circuit diagram of a solar cell model showing the different elements of Equation 7b as components in the circuit.....	14
6) An ideal cubic ABX_3 perovskite unit cell with blue A cations, yellow B cation, and red X anions.....	16
7) The $CH_3NH_3PbI_3$ crystal structure showing relative size of the $CH_3NH_3^+$ cation	18
8) Solar cell cross-section diagrams of a) planar $n-i-p$ and b) planar $p-i-n$ (inverted) heterojunction device architectures	20
9) The Shockley-Queisser Limit curve as seen on a PCE vs band gap plot	25
10) V_{OC} vs band gap plot showing the S-Q Limit and values for various current solar cell technologies	26
11) The unit cells of crystalline a) γ -CuI, b) Cu_2O , and c) CuO	29
12) The a) architecture and b) band diagram of a $CH_3NH_3PbI_3$ perovskite solar cell device with a CuI HTL with the same c) and d) respectively for a device with a Cu_2O HTL.....	34
13) ITO (in blue) anode pattern printed on glass to fit 4 devices per slide	34

14) The Cu-based HTL fabrication process showing the a) spin coating, b) NaOH dip, and c) thermal annealing steps	36
15) AFM images of CuI HTLs deposited at a) 30, b) 20, and c) 10 mg/ml precursor solution concentrations	40
16) AFM images of copper oxide HTLs processed from CuI including a) Cu ₂ O, b) CuO (250 °C annealing), and c) CuO (350 °C annealing) samples.....	40
17) Bar graphs of a) root mean square roughness, and b) maximum vertical displacement measured by AFM.....	41
18) A schematic diagram of a stylus profilometer measurement setup along length <i>l</i> , with scan axis, <i>x</i> , and displacement axis, <i>z</i>	42
19) Profilometer results showing averages for CuI, Cu ₂ O, and CuO samples of different thicknesses controlled by precursor solution concentration.....	43
20) Schematic diagrams of a) conceptual, b) semi-in-lens objective, and c) in-lens objective SEM lens arrangements.....	46
21) SEM cross-section image of a completed device with a Cu ₂ O HTL showing all layers. Note that the ITO/Cu ₂ O interface may not be visible	47
22) Planar SEM images of a) CuI, b) Cu ₂ O, c) CuO (250 °C annealing), and d) CuO (350 °C annealing) HTL samples.....	47
23) Comparison of EDS measured vs calculated atomic percentage results for a) CuI, b) Cu ₂ O, and c) 250 °C and d) 350 °C annealed CuO samples	50
24) Schematic diagram of UV-Vis experimental setup showing all equipment components	52
25) UV-Vis transmittance data for CuI, Cu ₂ O, CuO, and PEDOT:PSS HTL samples deposited on glass/ITO	53
26) UV-Vis absorbance data for CuI, Cu ₂ O, and CuO HTL samples deposited on glass/ITO	54

27) Geometric diagram of x-rays scattering off atomic planes causing diffraction according to Bragg's Law	56
28) XRD pattern for a CuI HTL sample clearly showing the {111} family of planes, indicating strong γ -phase crystallinity	57
29) XRD pattern for a Cu ₂ O sample showing only noise, indicating amorphous morphology	58
30) Schematic diagram of SE experimental setup showing polarization components and interaction with sample surface	59
31) a) Refractive index, n , and b) extinction coefficient, k , profiles for the various HTLs and substrate materials modeled by CompleteEASE software	64
32) J-V curve for champion glass/ITO/CuI/CH ₃ NH ₃ PbI ₃ /C ₆₀ /BCP/Al device with inset performance values	68
33) J-V curve for champion glass/ITO/Cu ₂ O/CH ₃ NH ₃ PbI ₃ /C ₆₀ /BCP/Al device with inset performance values	69
34) J-V model for champion glass/ITO/CuI/CH ₃ NH ₃ PbI ₃ /C ₆₀ /BCP/Al device with inset fitted resistivity and ideality factor values.....	75
35) J-V model for champion glass/ITO/Cu ₂ O/CH ₃ NH ₃ PbI ₃ /C ₆₀ /BCP/Al device with inset fitted resistivity and ideality factor values.....	76
36) J-V curve deviation for glass/ITO/CuI/CH ₃ NH ₃ PbI ₃ /C ₆₀ /BCP/Al device population average	77
37) J-V curve deviation for glass/ITO/Cu ₂ O/CH ₃ NH ₃ PbI ₃ /C ₆₀ /BCP/Al device population average	78

LIST OF ABBREVIATIONS

	Page
PCE: Power Conversion Efficiency	1
UV: Ultraviolet.....	1
CdTe: Cadmium Telluride	4
CIGS: Copper Indium Gallium Selenide.....	4
NREL: National Renewable Energy Laboratory.....	5
<i>p-n</i> : <i>p</i> -type <i>n</i> -type semiconductor.....	6
J-V: Current-Voltage.....	7
kT/q : Thermal Voltage	11
<i>p-i-n</i> : <i>p</i> -type intrinsic <i>n</i> -type semiconductor	12
J_{SC} : Short Circuit Current.....	12
V_{OC} : Open Circuit Voltage	12
r_{sh} : Shunt Resistivity.....	13
r_s : Series Resistivity	13
$J(V)$: Total Photovoltaic Current Function	14
J_0 : Diode Reverse Saturation Current	14
J_L : Total Photovoltaic Current Under Illumination	14
A : Ideality Factor	14
CaTiO ₃ : Calcium Titanate	16

CH ₃ NH ₃ PbBr ₃ : Methylammonium Lead Bromide.....	17
CH ₃ NH ₃ PbI ₃ : Methylammonium Lead Iodide.....	17
CH ₃ NH ₃ ⁺ : Methylammonium Ion	18
<i>n-i-p</i> : <i>n</i> -type intrinsic <i>n</i> -type semiconductor	20
TCO: Transparent Conductive Oxide.....	20
ITO: Indium Tin Oxide.....	21
Au: Gold.....	21
Ag: Silver	21
Al: Aluminum.....	21
HTL: Hole Transport Layer.....	21
ETL: Electron Transport Layer	22
FF: Fill Factor.....	23
S-Q: Shockley-Queisser	24
Cu-based: Copper-based.....	27
CuI: Copper Iodide.....	27
Cu ₂ O: Copper (I) Oxide	27
PEDOT:PSS: Poly(3,4-ethylenedioxythiophene) Polystyrenesulfonate	27
CuO: Copper (II) Oxide	27
<i>T</i> : Temperature.....	29
BCC: Body-Centered Cubic.....	30

FCC: Face-Centered Cubic	30
DI: Deionized	35
CO ₂ : Carbon Dioxide	35
PTFE: Polytetrafluoroethylene.....	35
RPMs: Rotations Per Minute	35
N ₂ : Nitrogen	35
PPM: Parts Per Million.....	35
NaOH: Sodium Hydroxide.....	35
NaI: Sodium Iodide	35
PbI ₂ : Lead Iodide	37
CH ₃ NH ₃ CH ₃ COOH: Methylammonium Acetate.....	37
CH ₃ NH ₃ I: Methylammonium Iodide.....	37
DMF: Dimethylformamide.....	37
BCP: Bathocuproine.....	38
AFM: Atomic Force Microscopy	39
R_{max} : Maximum Vertical Displacement Roughness	40
R_q : Root Mean Square Roughness.....	40
SEM: Scanning Electron Microscopy	45
FIB: Focused Ion Beam.....	46
EDS: Energy Dispersive X-Ray Spectroscopy.....	48

UV-Vis: Ultraviolet-Visible Spectroscopy	51
kT : Thermal Energy	54
XRD: X-Ray Diffraction Crystallography	55
SE: Spectroscopic Ellipsometry	58
k : Extinction Coefficient.....	60
n : Refractive Index	60

ABSTRACT

Methylammonium lead iodide perovskite solar cells have attracted much research attention in the last decade due to skyrocketing device performance and very low cost of production. However, despite great improvements in these devices, many of their commonly used constituent materials have stability issues that contribute to limiting the lifetime and performance of the solar cell. One device component that has been scrutinized recently is the hole transport layer, which has often been made from expensive and unstable conductive organic polymers such as poly(3,4-ethylenedioxythiophene) polystyrenesulfonate. This work attempts to replace the hole transport layer of a methylammonium lead iodide perovskite solar cell with an inorganic copper-based compound while still maintaining device performance and ease of sample processing. The particular materials studied for this are copper iodide and copper oxide. The layer processing for solar cell devices included single-step solution spin coating, low temperature thermal annealing, and thermal evaporation. Hole transport layer samples were characterized by several analysis techniques that revealed the relevant physical and electrical properties. Photovoltaic cells were characterized for device performance metrics by current-voltage analysis under AM1.5G simulated solar illumination. Device parameters that could not be directly observed were calculated by fitting measured curves to a current-voltage curve model. Results confirm that copper iodide and copper oxide thin films are a viable hole transport layer option for organic perovskite photovoltaic cells

with performance results matching or exceeding those of devices using a poly(3,4-ethylenedioxythiophene) polystyrenesulfonate hole transport layer.

I. INTRODUCTION

A Brief History of Photovoltaic Technology

The photovoltaic effect is a physical process that occurs when a voltage and corresponding electric current is produced in a material exposed to electromagnetic radiation. This was first demonstrated experimentally by French physicist Edmond Becquerel in 1839 using a photochemical cell containing silver chloride in an acidic solution with platinum electrodes.¹ He published his findings in *Comptes rendus de l'Académie des Sciences* where it received little attention until the later half of the 19th century. In retrospect, this may seem like a landmark discovery in the history of photovoltaic devices, but Becquerel's cell was hardly a practical electrical technology and produced only enough voltage to illustrate the effect.

The first working solid-state photovoltaic cell was produced by American inventor Charles Fritts in 1884. The device consisted of a sheet of selenium coated in a thin gold film and was installed on a New York City rooftop (seen in Figure 1), making it the first solar cell array installed in history. Although Fritts's cell was surprisingly similar in form and function to modern semiconductor cells, it was only capable of producing a power conversion efficiency (PCE) of about 1% and could not have been practically used with the electric technology of the time to produce power on a reasonable scale.²

In 1900, German physicist Max Planck advanced a seemingly radical idea that electromagnetic radiation could only carry energy in quantized units. His theory would ultimately prove to resolve the Ultraviolet (UV) Catastrophe, a major conundrum in the scientific community at the time regarding the disparity between the predicted and



Figure 1: The world's first solar array, invented by Charles Fritts in 1884.²

experimentally observed spectrum of radiation emitted by a black body. Five years later, a young 26 year old physicist named Albert Einstein would apply these ideas to the interaction between photons (the energy quanta of light) and charged particles. Einstein's model not only gave an early quantum mechanical description of what would later be called the photoelectric effect, but also offered a consistent explanation and prediction for experimental results that had been indecipherable during the time of the UV Catastrophe. Despite producing large bodies of other laudable physics works, both Planck and Einstein would go on to win the Nobel Prize in Physics (Planck in 1918 and Einstein in 1921) for their work pertaining to light energy quanta.^{3, 4}

The solar cell concept would continue to develop with advances in solid-state and

semiconductor physics throughout the 1930s and into World War II, but the global conflict would slow research focus on technologies that were considered non-essential to the war effort. As a result, the theory behind the photodiode would not be fully conceived until after the war. The first patent of a modern semiconductor photovoltaic cell was awarded in 1946 to Russel Ohl at Bell Labs while he was working on research that would contribute to the development of the first transistor.⁵

On April 25th, 1954, the first practical silicon-based cell was demonstrated by a research group at Bell Labs that included Daryl Chapin, Calvin Fuller, and Gerald Pearson. The observed PCE of the device was around 6%, a monumental improvement above all previously recorded photovoltaic cells.⁶ Although the first generation of silicon cells to follow were expensive to produce and not easily commercialized, they provided the first reliable validation that solar power systems could be practically manufactured and incorporated for a variety of applications. Not long after, Vanguard 1 became the first solar powered spacecraft in 1958.⁷ Other practical applications in military, industrial, commercial, and civilian sectors would soon follow.

Cost, Performance, and Practicality of Modern Solar Cells

The average cost per watt (adjusted for inflation to 2016 US dollars) of silicon-based solar power has fallen from \$79.29 in 1977 to less than \$0.30 in 2016.^{8,9} This exponential drop in cost, referred to as Swanson's Law,¹⁰ is of particular importance in 21st century energy production as solar power is now cheap enough to compete with fossil fuel energy sources that are major contributors to climate change such as oil, gas,

and coal. Alongside this development, the PCE of common commercially available solar cells has increased from around 4% in the 1970s to around 15% within the last few years. The highest quality commercial cells are even capable of a PCE greater than 20%.¹¹ This improvement in cost and performance of photovoltaic cells has been driven both by advancement in semiconductor processing technologies as well as the use of materials other than silicon.

Cadmium telluride (CdTe) thin film solar cells have been researched since the 1950s and are currently the only thin film photovoltaic power technology that can compete with the low cost of silicon based cells when used in large installations. The very low cost of mass manufacturing CdTe cells has made them of interest lately, but at about \$0.50 to \$0.60 per watt in 2016, they still are slightly more expensive than silicon cells in general and are not as practically priced for small installations such as a household rooftop. Furthermore, both cadmium and tellurium are highly toxic as is the chemical processing required to create CdTe solar cells. Manufacturers have attempted to reduce this environmental hazard by recycling old cells.¹²

Another thin film technology that has seen a recent rise in commercialization is copper indium gallium selenide (CIGS). CIGS cells shares many of the same cost saving benefits for manufacturing as CdTe cells. However, although the cost per watt is seemingly reasonable at \$0.55 to \$0.65 in 2016, CIGS has a cost to performance ratio generally inferior to that of silicon cells. This makes them less practical for larger installations and therefore limiting the mass market for them.¹²

In a rare and specialized class of their own are the multi-junction solar cells.

Employing a variety of ultra-high vacuum vapor deposition, epitaxial growth, and other pristine nanofabrication techniques, manufacturing even a single panel device can cost millions of dollars. When roughly translating their cost to price per watt, they are a staggering \$15 or more as of 2016. Their most notable quality, however, is their unrivaled power to weight ratio and PCEs in excess of 45%. Due to the extremely high cost, quality, and difficulty of manufacturing, multi-junction cells are only used in applications where power systems maintenance is impossible, such as on spacecraft.¹²

An important consideration of each of the solar technologies above is the pace of technological development compared to the improvement in unit price. The National Renewable Energy Laboratory (NREL) publishes a yearly chart that tracks improvement in photovoltaic device PCE over time for a variety of different solar cell technologies, including those discussed above. In viewing Figure 2, one can see the overwhelming trend in increasing PCE occurs over several decades regardless of the chosen material.

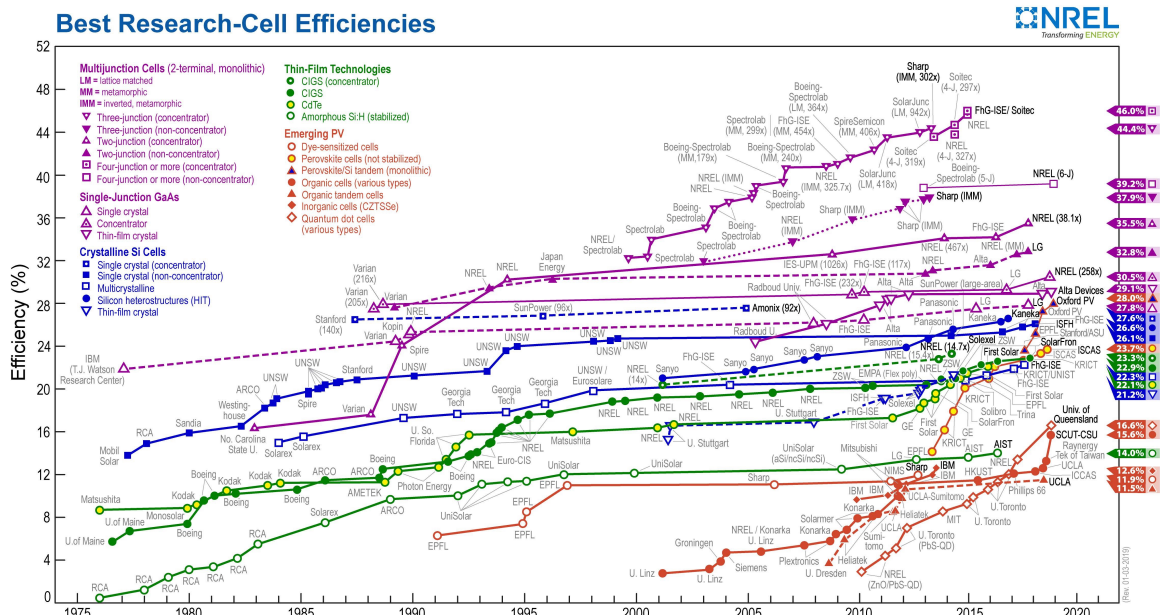


Figure 2: NREL Solar Cell Technology Efficiency Chart.²⁵

However, there is one notable exception to this, which is the organic perovskite based solar cell. This class of photovoltaic materials, only discovered and practically demonstrated within the last decade, has seen skyrocketing improvement in PCE while maintaining very low cost of fabrication for the experimental cells produced. To understand what made this rapid development possible, a general introduction to perovskite materials, as well as their application to photovoltaic technology, will be a necessary topic of discussion in a later section of this work. However, before the specifics of perovskite photovoltaics can be analyzed, it will be helpful to develop a general understanding of the physics and principles of operation of a solar cell.

Physical Principles of Operation for an Ideal Photodiode

A solar cell is a particular variety of a more general class of semiconductor device known as a photodiode. A photodiode is itself a particular kind of diode which is one of the foundational components of modern electronic devices. While early diodes primarily relied on large vacuum tube designs, most modern diodes are made from semiconductor materials joined in a p - n junction. The junction is named for the interface formed by a juxtaposition of material with excess holes (the p -type section) and material with excess electrons (the n -type section). A basic understanding of this type of diode is necessary before a complete model of a photodiode can be explored.

The defining characteristic of all diodes is the effective conduction of electric current in only one direction. With Ohm's Law in mind, an ideal diode is defined as having zero resistance in the forward current direction and infinite resistance in the

reverse current direction.¹³ This model is useful in conceptualizing the directional current operations of a diode, but is far from practical when analyzing current-voltage (J-V) measurements in the real world. To formulate an accurate model, a more detailed approach is required that accounts for charge carrier transport in the region near the junction. This region is often referred to as the depletion or space-charge region.

In 1949 while working at Bell Labs, William Bradford Shockley published an article which gave a detailed mathematical derivation for a model of p - n diode current.¹⁴ The resulting equation is now known as the Shockley Diode Equation or more generally as the Diode Law. To avoid confusion with the ideal diode presented in the previous paragraph, an ideal diode that follows the Diode Law will henceforth be referred to as a Shockley diode. With only minor extensions, Shockley's model can accurately account for nearly all of the observed phenomena of a p - n junction diode and continues to be the primary mathematical approach used to describe the physics of diode operation.¹⁵

In constructing the Diode Law, Shockley made the following four important assumptions: 1) the diode is an abrupt p - n junction and is charge neutral outside the depletion region, 2) charge carrier concentrations at the depletion region boundaries are related to the potential distribution via a Boltzmann relation, 3) changes in minority carrier concentration near the depletion region boundary are significant while changes in majority carrier concentration are negligible, and 4) both the electron and hole current densities are constant throughout the depletion region.¹⁴ A schematic diagram of an ideal Shockley diode is shown in Figure 3. The first assumption simplifies the geometry of the junction, treating the p -type and n -type sections of the diode as being in direct physical

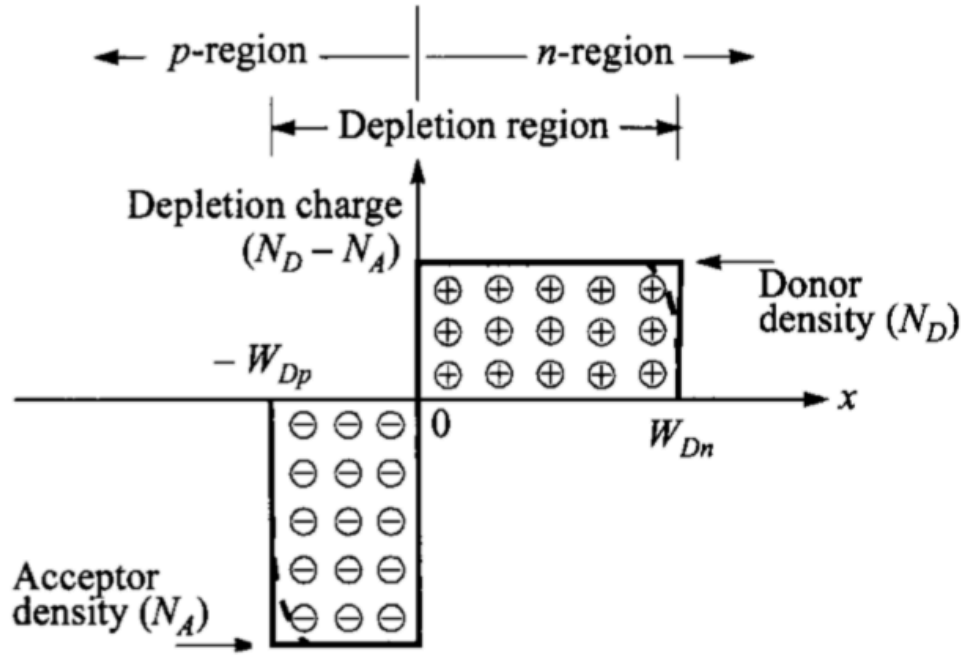


Figure 3: Schematic diagram of an ideal p - n junction diode illustrating the parameters of the depletion approximation.¹⁵

contact with one another at each point in a perfect plane. This arrangement defines an abrupt junction and has proven to be a reasonable approximation of the junctions found in real semiconductor diodes. The second assumption applies Maxwell-Boltzmann statistics to charge carrier transport in the diode, relating carrier concentrations to the potential across the depletion region. Such Boltzmann relations were known to be valid for non-degenerate semiconductors and were already in common usage when the Diode Law was first derived. The third assumption, commonly referred to as low injection conditions, is based on the fact that majority and minority carrier concentrations differ by several orders of magnitude in a section of semiconductor doped with one type of charge carrier. Thus, a significant change in minority carrier concentration at the depletion region boundary will still amount to approximately zero change in the corresponding majority carrier concentration. Consequently, it is the minority carrier current densities that dominate

Shockley diode operation. The fourth assumption simplifies the total current in the depletion region to ignore recombination and generation of carriers, which should be negligible in a Shockley diode.¹⁵ However, there are extensions to Shockley's model (to be discussed later in this section) which eliminate the need for this assumption and allow for other current effects to be considered.

As the complete derivation of the Diode Law employed by Shockley is beyond the scope of this work, a brief summary of the central concepts and equations will be provided before the law itself is examined. The derivation can be broken into three parts: 1) solving for properties in the depletion region, 2) solving for properties of the neutral regions, and 3) solving for the total current.¹⁴ The first part requires solving a Poisson Equation that, when extended to the known charge distribution in the given p - n diode, becomes a boundary value problem that yields the electric potential and field functions in the depletion region. The particular Poisson Equation relevant to modeling a Shockley

$$-\frac{d^2\phi}{dx^2} = \frac{dE}{dx} = \frac{\rho(x)}{\epsilon} = \frac{q}{\epsilon}(p(x) - n(x) - N_A + N_D) \quad (1)$$

diode is shown in Equation 1. It relates the electric potential, $\phi(x)$, the electric field, $E(x)$, and the charge density, $\rho(x)$, across the depletion region of a p - n junction. The conventional treatment in semiconductor physics is to define charge density as being the sum of the following components: the hole density, $p(x)$, the electron density, $n(x)$, the p -type dopant concentration, N_A , and the n -type dopant concentration, N_D . The elementary charge, q , and permittivity of the semiconductor, ϵ , also appear as physical constants. In a Shockley diode, the charge density is idealized on each side of the p - n junction (Shockley's first

assumption) so that N_A is constant in the p -type section and zero in the n -type section and N_D is constant in the n -type section and zero in the p -type section. Furthermore, both $p(x)$ and $n(x)$ are both zero across the depletion region (Shockley's fourth assumption). This simplification is commonly known as the depletion approximation.¹⁵

The second part of deriving the Diode Law requires solving a continuity equation that yields the minority carrier distributions in the neutral regions of the p - n junction.

When considering charge transport in a semiconductor, such continuity equations generally include drift, diffusion, generation, and recombination terms. For a Shockley diode, this equation can be simplified by recalling that the electric field is zero and the majority carrier concentration is fixed in the neutral regions. Thus the contributions to total current are only diffusion and minority carrier recombination (Shockley's third assumption). The resulting diffusion equation is Equation 2. It relates the hole concentration in the n -type neutral region, p_n , the equilibrium hole concentration, p_{n0} , and the hole diffusion length, L_p . The same equation for electrons in the p -type neutral region

$$\frac{d^2 p_n}{dx^2} = \frac{(p_n - p_{n0})}{L_p^2} \quad (2)$$

can also be obtained by simply exchanging the notation for letters n and p . The solution to the diffusion equation is then found by applying boundary conditions established above for carrier concentrations at the edge of the depletion region and the adjacent metal contact.¹⁴ The solution for the holes in the n -type neutral region is shown here in

$$(p_n - p_{n0}) = p_{n0}(e^{qV/kT} - 1)e^{(x-W_{Dn})/L_n} \quad (3)$$

Equation 3. Notice that a Boltzmann factor term, $e^{qV/kT}$, arises due to the Boltzmann

relation applied at the depletion region boundaries (Shockley's second assumption). This includes the thermal voltage, kT/q , conventionally treated as having a constant value of 25.9 mV at room-temperature, $T = 300$ K, as well as the voltage bias applied to the diode, V . This shows that the minority carrier concentrations at the boundaries between the depletion region and the neutral regions are controlled by the voltage applied to the diode.

The final part of deriving the Diode Law requires taking the minority carrier distributions found above and relating them to the minority carrier currents in the neutral regions. The hole and electron minority carrier currents respectively are shown in Equation 4. These can then be added to give the total current through the diode. The

$$J_p = -qD_p\left(\frac{dp_n}{dx}\right) \quad J_n = qD_n\left(\frac{dn_p}{dx}\right) \quad (4)$$

total current equation is shown in Equation 5 without any simplification so the

$$J = J_p + J_n = \left(\frac{qD_p p_{n0}}{L_p} + \frac{qD_n n_{p0}}{L_n}\right)(e^{qV/kT} - 1) \quad (5)$$

contributions to current from both holes and electrons can be seen. Since only diffusion currents are considered in this model, the diffusion coefficients for holes and electrons, D_p and D_n respectively, are the only remaining quantities that need to be incorporated to complete the derivation. By substituting the full diffusion current term with a single current density variable, J_0 , the result is the J-V relationship that defines a Shockley diode, the Diode Law, shown in Equation 6.¹⁵

$$J(V) = J_0(e^{qV/kT} - 1) \quad (6)$$

Recall that a diode is defined by effectively conducting current in only one

direction. It is clear from inspection that the derived Diode Law fits this behavior well. Negative voltage bias results in a small reverse current that quickly approaches a constant value, forward voltage bias results in an exponentially increasing current as more bias is applied, and at zero bias the diode conducts no current.¹³ Unfortunately, this means that no power can be extracted from such a device, so an extension to the Diode Law is required to properly model a solar cell.

The $p-n$ diode concept developed above can now be modified to include a wide intrinsic layer between the p and n -type layers. This $p-i-n$ architecture greatly expands the depletion region and requires a revision to the Diode Law in which Shockley's third and fourth assumptions no longer strictly apply. Since the intrinsic layer is not doped like the p and n -type sections on either side, a $p-i-n$ diode operates under high injection conditions where excess carriers (rather than minority carriers) dominate the electron and hole current densities. Furthermore, the restriction on recombination and generation in the depletion region will be removed so that charge generation in the intrinsic layer from photogeneration can now be included in the model. Such a device can now appropriately be called a photodiode, or for the purposes of this work, a solar cell.

Unlike the Shockley diode model on its own, solar cells have J-V characteristics that allow power to be extracted. This is made possible by the fact that the device produces a maximum measurable current at zero voltage bias, the short circuit current, J_{SC} , and a maximum measurable voltage at zero current, the open circuit voltage, V_{OC} . When comparing the J-V function of a standard diode to that of a solar cell, as shown in Figure 4, it can be seen that the effect of these new parameters is to shift the standard

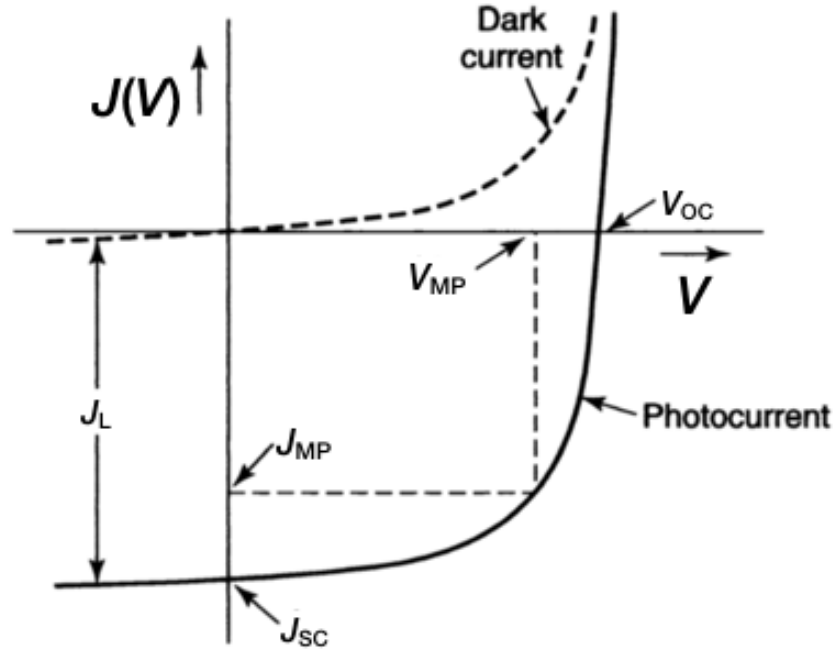


Figure 4: J-V curve of a solar cell in darkness (dotted curve) and under illumination (solid curve).¹⁶

diode curve to the lower-right portion of the graph. Since power is the product of voltage and current, a non-zero power output function now arises with maximum power at a critical point along the J-V curve.

It is now appropriate to modify the Diode Law equation established above so that it conforms to the experimentally relevant solar cell parameters. It is worth noting that this work uses two versions of the photovoltaic current equation, seen in Equations 7a and 7b, to model J-V curves and calculate values for some of these parameters. The only difference between these is that Equation 7a includes only shunt resistivity, r_{sh} , and

$$J(V) = J_0(e^{qV/AkT} - 1) - J_L + \frac{V}{r_{sh}} \quad (7a)$$

$$J = J_0(e^{q(V-Jr_s)/AkT} - 1) - J_L + \frac{V - Jr_s}{r_{sh}} \quad (7b)$$

ignores series resistivity, r_s , while Equation 7b includes both resistivities. The benefit

of Equation 7a is that it can be solved explicitly for the total photovoltaic current function, $J(V)$, whereas Equation 7b cannot. Both equations treat the total current as resulting from multiple components wired together in a circuit. A circuit diagram of this multicomponent device can be seen in Figure 5 and obeys Kirchhoff's Laws and other tenants of circuit analysis. Other parameters included in these equations are the diode reverse saturation current, J_0 , the photocurrent produced by the cell under illumination, J_L , and the ideality factor, A . Each of these parameters, and the real device effects they attempt to account for, will now be elaborated on.

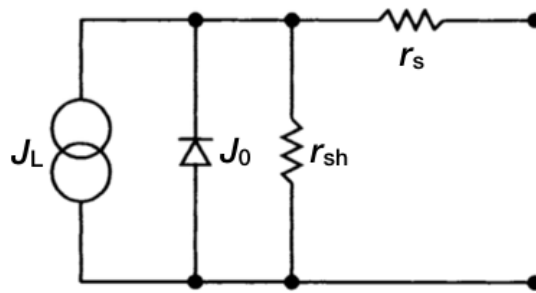


Figure 5: Circuit diagram of a solar cell model showing the different elements of Equation 7b as components in the circuit.¹⁶

Shunt resistance is a phenomena that most often occurs due to undesirable shorting within the device. It produces a low resistance pathway for charge carriers to conduct that is parasitic to the photocurrent. As a result, shunt resistance induces a slope in the flat portion of the J-V curve, near the point of J_{SC} , which reduces the maximum PCE. It behaves most like a resistor added in parallel to the solar cell circuit diagram.

Series resistance, as applied to the photovoltaic current equation, accounts for the general resistance across the solar cell components. It attempts to address the resistances that arise within insufficiently conducting electrodes or within bulk materials devoid of excess charge carriers. It results in a reduction of the slope of the J-V curve past the

exponential bend, near the point of V_{OC} , which also has a negative impact on maximum PCE. For purposes of this work, series resistance is excluded from the photovoltaic J-V curve modeling as the real device curves to be discussed later are appropriately fitted without it.

The final parameter to discuss is the ideality factor. In mathematical terms, it determines how sharp the exponential bend in the J-V curve is. Physically, it is meant to represent the effects of recombination within the device. The Diode Law, in which recombination only occurs in the bulk regions, always has A equal to 1. When including depletion region recombination, A is theoretically expected to fall between 1 and 2.¹⁶ In real solar cells, A can exceed 2, indicating additional recombination mechanisms.¹⁷ Such mechanisms will merit further discussion in the conclusion section of this work as calculated ideality factors exceeded the theoretically expected range. As ideality factor increases, the J-V curve becomes less “square”, again reducing maximum PCE.¹⁶

With a valid photovoltaic current model now in place, it is time to focus on the specific material components of a real organic perovskite solar cell. However, this requires that an overview of perovskite materials be given first. This topic will be addressed in the next section.

Introduction to Perovskites and Application to Photovoltaics

The mineral perovskite was discovered by German mineralogist Gustav Rose in 1839 and was later named after Lev Perovski, a Russian geologist who was a founding member of the Russian Geological Society.¹⁸ The raw mineral largely consists of calcium

titanate (CaTiO_3) which forms in an atomic arrangement now known as the perovskite structure. In general, a perovskite is any crystalline material with a cubic unit cell consisting of ABX_3 , where A represents cations at the corners of the cube, B represents a cation at the body center, and X represents anions at the face centers.¹⁹ An illustration of an ideal perovskite unit cell is shown in Figure 6.

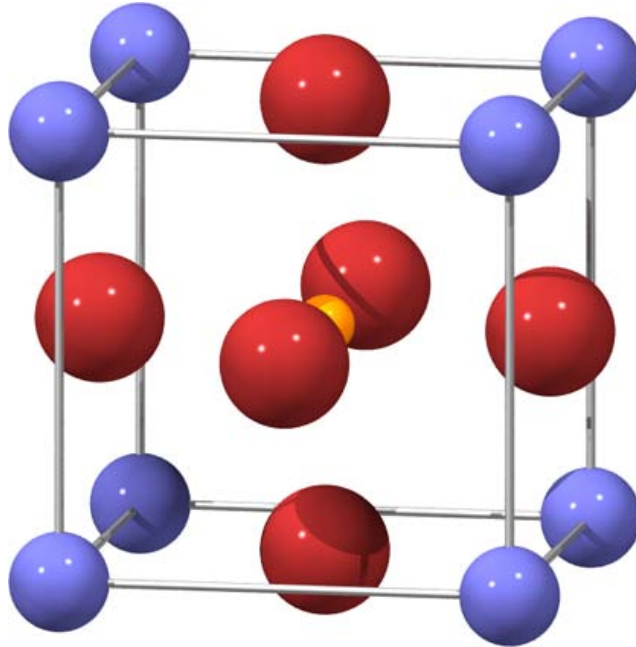


Figure 6: An ideal cubic ABX_3 perovskite unit cell with blue A cations, yellow B cation, and red X anions.¹⁹

A unitless tolerance factor, t , is calculated from a geometric relationship between the ionic radii, r_A , r_B , and r_X , and is used to quantify the degree of distortion in the lattice. For an ideal cubic perovskite, t equals exactly 1. This relationship, shown in Equation 8, is known as the Goldschmidt Rule.²⁰ The lattice maintains a stable cubic structure for tolerance factor values in the range of $0.8 \leq t \leq 1.0$. As the tolerance factor is reduced to

$$t = \frac{1}{\sqrt{2}} \frac{(r_A + r_X)}{(r_B + r_X)} = 1 \quad (8)$$

less than 0.8, the unit cell rescales due to lattice distortions and the cubic structure

approaches orthorhombic. As the tolerance factor is increased to above 1.0, the lattice distortions disrupt the 3D cubic structure sufficiently for it to behave more like weakly interacting 2D hexagonal layers.²¹ Further details of the specific perovskite species important to this work will be elaborated on in the next section.

Perovskites are now a well-studied class of materials that exhibit a wide variety of interesting physical and electrical properties including ferroelectricity, magnetoresistance, piezoelectricity, and superconductivity.²² While research into perovskite materials is many decades old, however, its applications to photovoltaic technology only began in 2009. As first reported in *Kojima et al.*, methylammonium lead bromide ($\text{CH}_3\text{NH}_3\text{PbBr}_3$) and methylammonium lead iodide ($\text{CH}_3\text{NH}_3\text{PbI}_3$) were found to be effective visible light spectrum sensitizers for a photochemical cell that yielded a PCE of 3.8% and was stable for only a few minutes.²³ Improvements on this concept, especially the creation of solid-state *p-i-n* heterojunction architectures, allowed for organic perovskite thin film cells to exceed 10% PCE by 2014.²⁴ As of January 3rd, 2019, the highest performing organic perovskite cell has reached a PCE of 23.7%.²⁵

In addition to the meteoric rise in device PCE observed in recent years, organometal halide perovskite solar cells also enjoy a very low cost of fabrication thanks to common cheap precursors and use of simple deposition techniques like solution spin coating and thermal evaporation. Although not all processing used to make experimental cells can scale well for mass manufacturing, the cost and abundance of precursor materials continues to make organic perovskites an attractive renewable energy material with much commercial potential.²⁶ The only serious hurdle that continues to prevent its

practical marketability is an abundance of degradation pathways that rapidly compromise the organic perovskite structure, often in less than 24 hours.²⁷ While stability concerns continue to be an important topic of study in this emerging technology, the focus of this work is given mostly to device architecture and its motivations. The next section will elaborate on the crystal structure and desirable characteristics of the perovskite species utilized in this work, $\text{CH}_3\text{NH}_3\text{PbI}_3$.

$\text{CH}_3\text{NH}_3\text{PbI}_3$ Crystal Structure and Useful Properties

$\text{CH}_3\text{NH}_3\text{PbI}_3$ follows the same perovskite structure presented in the previous section. It is composed of the following ionic components: A) CH_3NH_3^+ , B) Pb^{+2} , and X) I^- . A diagram of this organic perovskite crystal structure can be seen in Figure 7. Notice that the polyatomic CH_3NH_3^+ ion takes up significantly more volume than the other

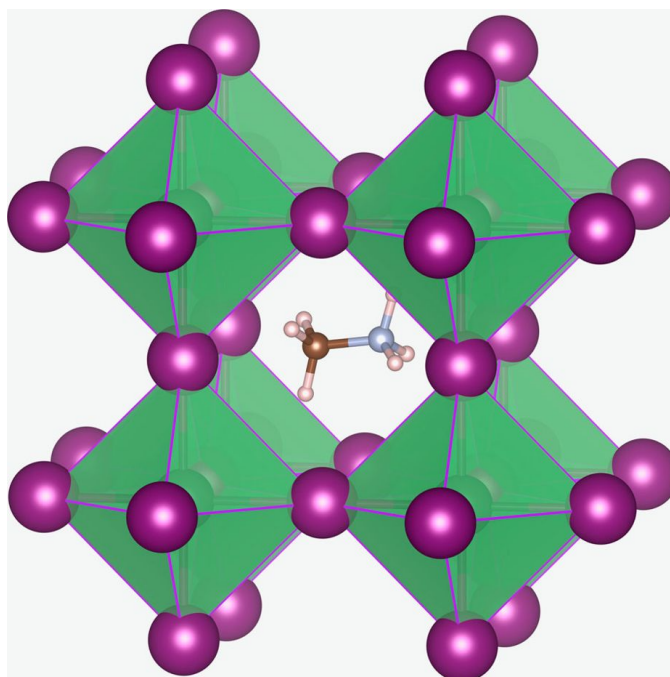


Figure 7: The $\text{CH}_3\text{NH}_3\text{PbI}_3$ crystal structure showing relative size of the CH_3NH_3^+ cation.⁴²

monoatomic ions. This causes the cubic lattice constant, which is approximately 6.3 Å at 300 K,²⁸ to be appreciably larger than perovskite species with only monatomic ions, such as CaTiO₃ (which has a lattice constant of approximately 3.8 Å at 300 K).²⁹ It also is partially responsible for making the lattice less stable and more prone to defects that can affect electrical characteristics.²¹

When considering semiconductor properties, CH₃NH₃PbI₃ has many desirable features that make it practical as the intrinsic layer in a *p-i-n* photodiode. The charge carrier mobilities, μ , are sufficient enough ($\mu_e = 66 \text{ cm}^2/\text{V/s}$ and $\mu_h = 105 \text{ cm}^2/\text{V/s}$) that the material can conduct both electrons and holes, a necessary feature for conducting and collecting photoelectrically separated charges.^{17, 30} Furthermore, the band gap of CH₃NH₃PbI₃, which has been experimentally measured at 1.55 eV,³¹ is close to the band gap that theoretically maximizes absorption of the solar spectrum, at 1.34 eV.³² This allows the perovskite layer to collect most solar radiation in the UV to infrared range, which optimizes solar cell performance.

It is important to keep in mind that the single crystal description of CH₃NH₃PbI₃ offered above is generally only useful in understanding its basic physical properties. Real organic perovskite thin films are most often polycrystalline in morphology, which brings about additional device fabrication considerations.¹⁷ These concepts, and the other architecture specifics important to engineering a working organic perovskite solar cell, will be explored in the next section.

II. ORGANIC PEROVSKITE PHOTOVOLTAICS

Anatomy of an Organic Perovskite Photovoltaic Cell

With physical principles of operation and organic perovskite material characteristics now established, it is time to focus on assembling a practical organic perovskite solar cell from the fundamental building blocks of a photodiode. The general architectures for planar $n-i-p$ heterojunction and planar $p-i-n$ heterojunction (also called inverted) solar cells³³ can be seen in Figures 8a and b respectively. This requires a closer look at each of the layers that make up such a device, as well as the interfaces between these layers. To begin this exercise, the electrodes on either side of the diode will be treated first.

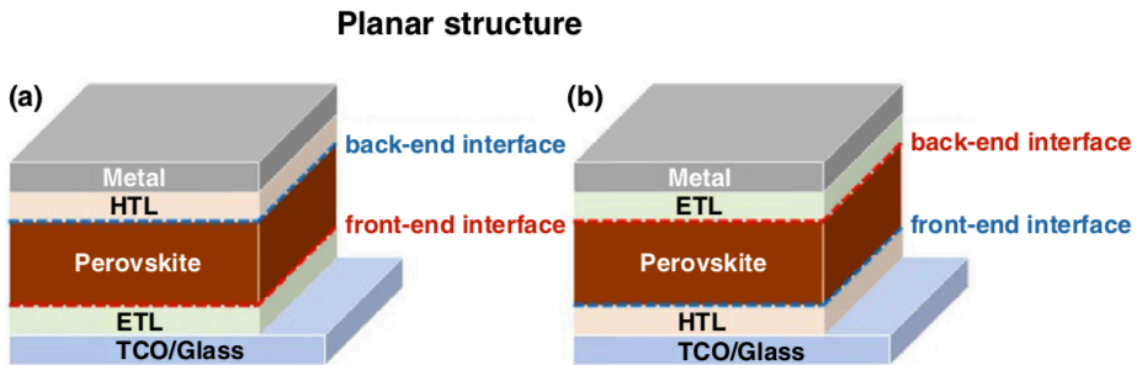


Figure 8: Solar cell cross-section diagrams of a) planar $n-i-p$ and b) planar $p-i-n$ (inverted) heterojunction device architectures.³³

In order for a solar cell to operate properly, sunlight needs to be able to reach the photoactive layer. This is only possible if either the cathode (for $n-i-p$) or anode (for inverted) are sufficiently transparent to the solar spectrum. Since the electrode that is deposited on the glass-side of the device should transmit most light wavelengths in the range of 400 to 800 nm, a wide band gap semiconductor material is required. The most common such electrode materials are transparent conductive oxides (TCO) such as

indium tin oxide (ITO). With the glass-side electrode material selected, the back-side electrode can then be made of any metal that can be easily deposited as a low resistance electrical contact, such as gold (Au), silver (Ag), or aluminum (Al). The interface of an electrode with the adjacent p or n -type layer should be flat and have a low defect density. This lowers series resistance and allows carriers to easily conduct into the contacts.^{33–35}

As the experimental solar cells produced in this work are only of the inverted planar heterojunction variety, the remainder of this section will be guided by the use of this architecture. With this in mind, the next layer to be treated will be the p -type layer, most often referred to as the hole transport layer (HTL), which is deposited on top of the transparent anode. Since the HTL is on the glass-side of the device, it too must effectively transmit light in the range of the solar spectrum. Furthermore, it must behave like an acceptor doped semiconductor with a high hole mobility and a sufficiently large conduction band offset that acts as a barrier to electrons.^{33, 34} This allows it to effectively conduct only holes.

The most important layer in the device architecture is, of course, the photoactive organic perovskite layer. As mentioned earlier, this layer is almost exclusively of polycrystalline morphology in real thin film solar cells. The need for clean interfaces with the transport layers requires that the intrinsic layer have low roughness and as few grain boundaries as possible. However, if a large-grained intrinsic layer is deposited, it will have a higher roughness due to the difference in size of adjacent grains. Conversely, a small-grained structure will have a low roughness as adjacent grains will be closer in size. As this runs contradictory to the desired roughness and presence of grain

boundaries, a compromise between these factors is required. This can be achieved by spin coating the perovskite layer using appropriate solution chemistry and solvent evaporation rate.³⁶ These considerations will be addressed by the perovskite ink formulation covered in the device fabrication section of this work.

Deposited on the back-side of the intrinsic layer is the electron transport layer (ETL). Since the light entering the glass-side of the device should be absorbed by the perovskite layer, the ETL need not be transparent. It must behave like an donor doped semiconductor with a high electron mobility and a sufficiently large valence band offset that acts as a barrier to holes.^{33, 34} This allows it to effectively conduct only electrons. For the devices made in this work, the ETL is actually composed of two materials, deposited one on top of the other. These materials will be discussed later when the fabrication procedures are covered.

The interfaces between the transport layers and the intrinsic perovskite layer should be as defect-free and abrupt as possible. This can be achieved by using materials with lattice constants that are nearly (ideally exactly) equal on either side of the interface. Common issues that occur at the transport/intrinsic layer interfaces are charge trapping and non-zero interfacial capacitances, both of which have a parasitic effect on total device photocurrent.^{16, 31} Such effects are magnified if the transport layers are made from amorphous materials that cannot produce clean interfaces with the perovskite and contain internal voids that can greatly hinder carrier mobilities.³⁴ This particular mechanism will become of interest later in this work as one of the HTL materials chosen is itself amorphous.

With the general anatomy of an organic perovskite solar cell now constructed, there are limitations on both fabrication and theoretical modeling that are worth a brief review. Such considerations will illustrate the connection between the photovoltaic J-V model employed above and the performance limits of real devices at the forefront of current research in this field. These will be covered in necessary detail in the next section.

Practical and Theoretical Limits of Organic Perovskite Solar Cells

The most important experimentally measurable parameter of solar cell performance is PCE. Although this has already been used to benchmark the quality of various types of cells discussed earlier in this work, the calculation of this quantity, and how it relates to the other quantities already introduced, has not yet been treated. As such, it is important that this be elaborated on before any experimental results can be considered.

The parameters responsible for making power output possible, J_{SC} and V_{OC} , have already been incorporated into the photovoltaic current model established earlier. These quantities have additional utility in calculating another necessary device parameter, fill factor (FF). FF is presented as a percentage that is effectively a measure of the “squareness” of the J-V curve, with 100% corresponding to a perfect right angle at the maximum power point, P_{max} , as was observed in the ideal diode model. It can be calculated as shown in Equation 9.¹⁶ A quick observation of the Shockley model shows that even a perfect Shockley photodiode does not have a FF of 100%. Thus, there are

$$FF = \frac{P_{max}}{J_{SC}V_{OC}} \quad (9)$$

fundamental limits to FF, even in theoretical devices.

With the tools necessary to calculate PCE, this quantity can now be defined as the ratio of generated power over the total power of the solar spectrum received on Earth, P_{Sol} . This calculation is shown in Equation 10.¹⁶ Note that the accepted value for P_{Sol} is 100 mW/cm².³²

$$PCE = \frac{J_{SC}V_{OC}FF}{P_{sol}} \quad (10)$$

Shockley's contributions to diode modeling and solar cells also includes a theoretical limit on maximum PCE possible for any $p-n$ junction based solar cell used on Earth. It is known as the Shockley-Queisser (S-Q) Limit, named in honor of Shockley and another solid-state physics pioneer, Hans-Joachim Queisser.³² The S-Q Limit will not be specifically covered in this work, but can briefly be described as including the following physical considerations: the energy at the peak of the solar spectrum (seen in Figure 9), the effects of black body radiation, the effects of charge recombination in the depletion region and elsewhere, and losses in the solar spectrum due to the atmosphere or the absorbance spectrum of materials used. The S-Q Limit for any single-junction solar cell has been calculated to be a PCE of 33.7%,³² while the S-Q Limit for organic perovskite based single-junction cells has been calculated to be a PCE of 30.1%.¹⁷ At the bleeding edge of current organic perovskite solar cell research are cells that produce a PCE in excess of 20%. However, as this is still well below the S-Q Limit, it is worth a

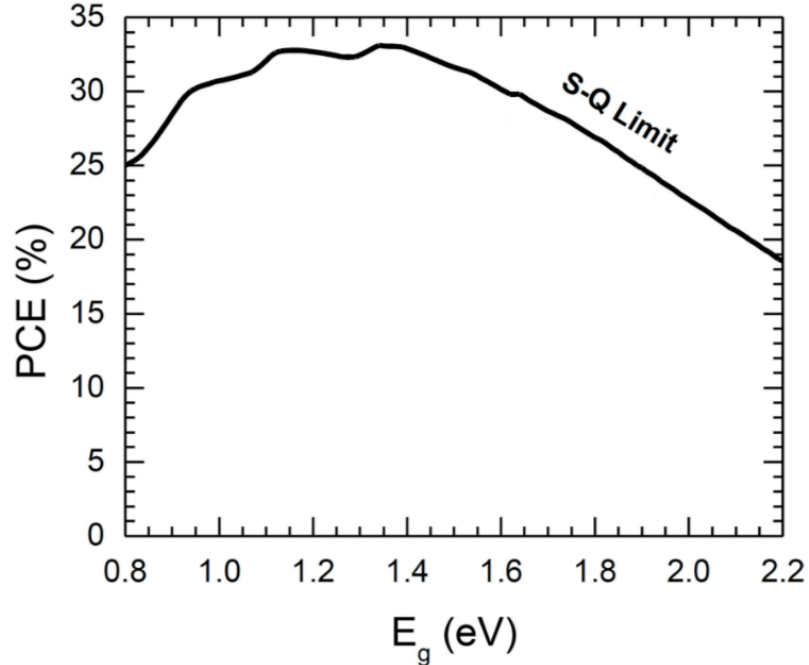


Figure 9: The Shockley-Queisser Limit curve as seen on a PCE vs band gap plot.¹⁷

quick review of what device parameters and practical considerations are restricting experimental cells from achieving their full potential.

Each of the following parameters assumes an organic perovskite with a 1.6 eV band gap. The theoretical limit on J_{SC} for organic perovskite cells is 25.47 mA/cm², which is only a small margin above that found in most high quality cells experimentally produced. The S-Q Limit on V_{OC} is 1.309 V,¹⁷ which is marginally higher than the maximum experimental value produced at 1.260 V.³⁷ An important item to note here is that maximum V_{OC} is limited by the band gap of the photoactive layer as shown in Figure 10. Band gap tuning organic perovskites to closer to 1.34 eV could be a possible avenue towards boosting the S-Q Limit and therefore PCE. However, most current research remains focused on optimizing J_{SC} and V_{OC} since there is still plenty of room for PCE improvement while keeping the band gap fixed around 1.6 eV.

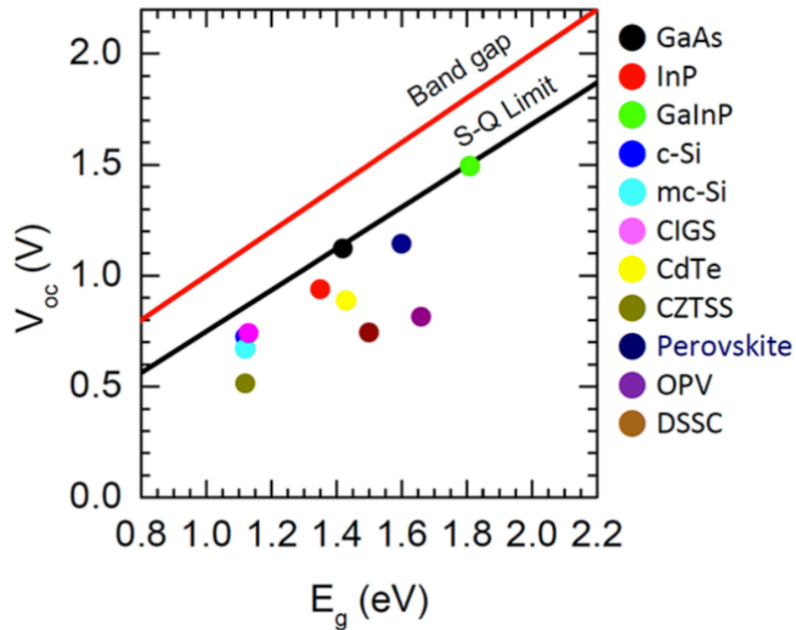


Figure 10: V_{OC} vs band gap plot showing the S-Q Limit and values for various current solar cell technologies.¹⁷

PCE is dependent on FF, J_{SC} , and V_{OC} , so it comes as no surprise that the maximum experimentally recorded FF of 80.1%³⁷ is far below the theoretical maximum of 90.5%.¹⁷ FF can also be limited by the ideality factor, which can practically never be much less than 2 in real devices. This is largely due to practical considerations when fabricating cells such as the crystallinity of layers and the quality of interfaces. Additionally, recombination effects in the intrinsic layer that cannot be eliminated can also limit how low the ideality factor can be.^{16, 17}

Beyond the mathematical and experimental parameters detailed above, there are additional aspects of device design that can hinder performance. Other practical considerations that are not explicitly tied to device parameters include surface and internal reflections of incident light, series resistances created by non-ideal conduction of device layers and/or contacts, and device defects caused by contamination during

fabrication.¹⁶ Though it is far from an exhaustive list, these considerations help illustrate the difficulty in making devices that inch closer and closer to the S-Q Limit. Although this work will not attempt to address most of these issues directly, it will seek to improve device performance by addressing one particular device layer, the HTL. This topic will be introduced in the next section.

In Pursuit of Better Hole Transport Layer

The central focus of this work will be to find a suitable inorganic HTL as a replacement for the more often used organic-based HTLs that are well known in current device fabrication research. This is of particular interest as organic HTLs often suffer from the same stability concerns that organic perovskite does itself. Despite such drawbacks, conductive organic polymers continue to be popular HTL materials in organic perovskite solar cells. This is largely due to them having desirable electrical characteristics such as a wide band gap and appropriate hole conductivity that make them attractive as natural *p*-type materials well suited for use as an HTL.³⁸ However, as will be specifically elaborated on in this work, there are two copper-based (Cu-based) inorganic compounds that share many of these characteristics while having additional benefits that organic polymers lack. These compounds are copper iodide (CuI) and copper (I) oxide (Cu₂O), which will be compared in this section to one of the most popular conductive polymers, poly(3,4-ethylenedioxythiophene) polystyrenesulfonate (PEDOT:PSS). Additionally, copper (II) oxide (CuO) will also be briefly investigated as it is the most stable form of the copper oxides observed in atmosphere.³⁹

As discussed earlier, the interfaces between device layers can be of specific concern when attempting to reduce device defects. As it turns out, this becomes particularly important when considering both the ITO/PEDOT:PSS and PEDOT:PSS/CH₃NH₃PbI₃ interfaces of devices with such an HTL. When examining the ITO/PEDOT:PSS interface, it has been reported that indium migrates into the PEDOT:PSS layer over time, a process which is greatly accelerated when the sample is left in normal atmosphere for only a few days. It is believed this occurs due to the hygroscopic nature of the PSS polymer which produces an acidic environment after it absorbs moisture from the air. The resulting acidity can be attributed to reactive functional groups that form along the PSS polymer chain which are susceptible to leeching the indium out of the ITO layer. This effectively causes the PEDOT:PSS layer to etch away the ITO over time.⁴⁰

When examining the PEDOT:PSS/CH₃NH₃PbI₃ interface, a similar hygroscopic mechanism can result in the degradation of the perovskite. In this instance, the PEDOT:PSS layer both chemically attracts (as stated above) and physically absorbs water (due to internal voids that act like a sponge) from the atmosphere. Once this moisture is trapped in the interface, the PSS again becomes acidic, this time reacting with the ionic components of the perovskite lattice. Additionally, the semi-porous nature of the PEDOT:PSS layer creates an interface with the perovskite that contains many possible charge trapping sites. These can increase the charge carrier recombination rate within the device⁴¹ as well as promote unwanted ion migration. Both of these effects can increase J-V hysteresis⁴² and other undesirable device characteristics.

With all these factors combined, it is easy to understand the motivation behind

seeking an inorganic HTL that can replace the use of PEDOT:PSS in organic perovskite solar cells. Although this work will not elaborate on organic conductive polymers other than PEDOT:PSS, many such polymers share similar stability concerns. With this in mind, focus will now be directed towards the Cu-based materials at the center of this body of research and how their characteristics measure against those of PEDOT:PSS. As was done for the perovskite crystal system, the crystal structure of CuI, Cu₂O, and CuO will be explored. Explicit attention will also be given to lattice matching between CH₃NH₃PbI₃ and each of these Cu-based materials as this directly contributes to the quality of the HTL/CH₃NH₃PbI₃ interface.

The unit cells for the crystal structures of γ -CuI, Cu₂O, and CuO can be seen in Figures 11a, b, and c respectively. Their associated lattice constants and interaxial angles will be covered below. Before expounding on these compounds individually, it should be noted that there exist three phases of CuI which will form at different temperatures (T) as follows: 1) γ -CuI which forms in the zinc blende structure at $T < 390$ °C, 2) β -CuI which forms in the wurtzite structure at 390 °C $\leq T < 440$ °C, and 3) α -CuI which forms in the rock salt structure at $T \geq 440$ °C. Of these, only the γ -CuI is used in this work.

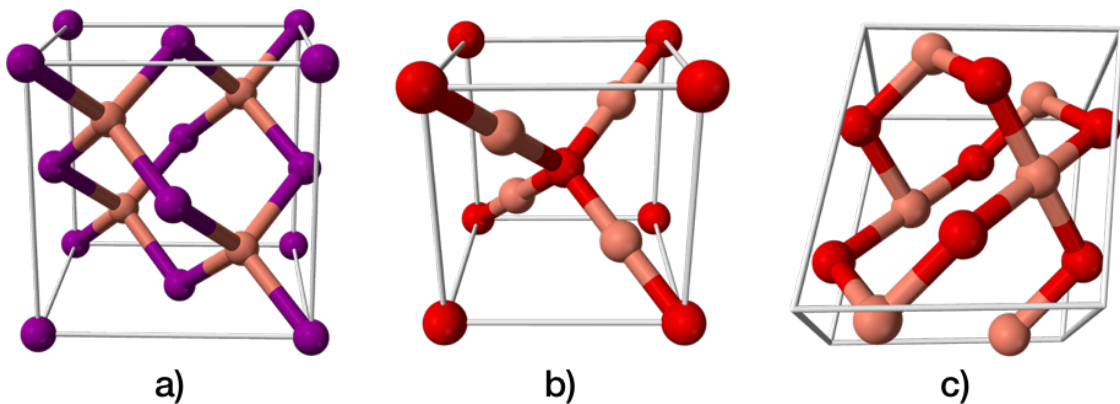


Figure 11: The unit cells of crystalline a) γ -CuI, b) Cu₂O, and c) CuO.⁴³⁻⁴⁵

When considering the logistics of device fabrication, one important goal of this research is to reduce the overall thermal budget wherever possible. Thus, for devices employing a CuI HTL, only the low temperature γ -phase is desirable. γ -CuI also has the additional benefit of having a lattice constant of approximately 6.1 Å,⁴³ which only differs from that of CH₃NH₃PbI₃ by -3.2%. As both γ -CuI and CH₃NH₃PbI₃ are of a cubic structure and have nearly equal lattice constants, these materials are naturally well suited to form an HTL/perovskite interface with a favorable geometry for reducing defects. Furthermore, as CuI already contains an abundance of iodide anions, the prevalence of iodide ion migration across the HTL/CH₃NH₃PbI₃ interface⁴² is likely reduced, thereby increasing the stability of both layers.

Cu₂O is a stable single phase of the more general material copper oxide and forms in the cubic crystal structure. The oxygen atoms are arranged in a body-centered cubic (BCC) sublattice while the copper atoms are arranged in a face-centered cubic (FCC) sublattice. With a lattice constant of approximately 4.3 Å,^{39, 44} the Cu₂O unit cell is in roughly a 2:3 linear ratio and a 1:3 volume ratio with the CH₃NH₃PbI₃ unit cell. Assuming that both materials are monocrystalline, such a lattice mismatch would put significant strain on the atomic bonding at the Cu₂O/CH₃NH₃PbI₃ interface. This would result in interfacial defects that would affect charge carrier mobility at the interface between the two materials. As will be discussed later, the actual Cu₂O HTLs created for this work were found to have an unexpected structure that produces complications beyond those addressed here.

CuO is another stable single phase of copper oxide that forms in the monoclinic

structure. It has three independent lattice constants of approximately 4.7, 3.4, and 5.1 Å with a vertical tilt of approximately 99.5°. ⁴⁵ Of the two forms of copper oxide, CuO is more thermodynamically stable than Cu₂O. ^{44, 45} Despite this, its crystal structure is poorly suited to interface with organic perovskite species. As such, no devices made for this research employed CuO HTLs, although thin film samples were made to compare material characterization results with that of Cu₂O. The specifics of this comparison will be elaborated on later in the characterization section of this work.

The guiding motivation behind the research presented here is to find a Cu-based HTL that is compatible in an organic perovskite photovoltaic device architecture and that is equal or superior to PEDOT:PSS in both electrical and physical characteristics. As the crystallographic properties of each of these compounds has already been discussed, the hole mobilities and band gaps of CuI, Cu₂O, CuO, and PEDOT:PSS are now worth inspecting. Table 1 contains the values of these parameters for each of the four materials listed. It should be noted that some of these values are based on theoretical calculations while others are based on experimental measurements of bulk materials. Furthermore, for the case of Cu-based compounds, these values also assume a single crystal material. Although these assumptions paint an over-idealized picture of the materials that are used in real solar cell devices, the magnitude of disparity between the mobilities and band gaps of these materials is enough to understand why a move away from PEDOT:PSS HTLs is

Table 1: The hole mobilities and band gaps of PEDOT:PSS, CuI, Cu₂O, and CuO.

	PEDOT:PSS ^{50, 51}	CuI ⁴⁶	Cu ₂ O ^{47, 48}	CuO ⁴⁷⁻⁴⁹
Hole Mobility	1.2×10 ⁻⁷ –3×10 ⁻⁵ cm ² /V/s	43.9 cm ² /V/s	4.3 cm ² /V/s	10 ⁻⁷ –1.5×10 ⁻⁵ cm ² /V/s
Band Gap	0.7–1.5 eV	3.1 eV	2.1 eV	1.0–1.5 eV

both necessary and possible. It should also be apparent from these values why CuO HTLs were not worth investigating for the purposes of this research.

Another item worth covering that has only briefly been mentioned is the implication of an HTL material's band gap. As the device architecture applied in this work is an inverted heterojunction solar cell, the HTL lies between the glass and the intrinsic layer. This means that, ideally, any light reaching the photoactive section of the device must be able to pass through the HTL without being absorbed or reflected.

When referencing the values in the table above, there are effectively three different band gap choices provided from the materials presented: 1.5, 2.1, and 3.1 eV. In general, photons with energy greater than the band gap are reflected or absorbed while photons with energy less than the band gap are transmitted. As photons in the visible spectrum range from energies of 1.7 eV (for red light) to 3.1 eV (for blue light),⁵² a material with a band gap of 1.5 eV will generally transmit less visible light than materials with higher band gaps. This also broadly explains why PEDOT:PSS and CuO thin films appear as transparent grey while Cu₂O and CuI thin films appear as transparent orange-yellow and blue-violet respectively. The transmittance spectra of all these materials will be discussed in detail later when covering HTL characterization data.

In addition to band gap considerations, the location of band edges was also an important factor in choosing CuI and Cu₂O as inorganic HTL materials. When examining the transport of holes from the intrinsic layer and through the HTL, the difference in the valence band edge between layers is of particular interest. This is because larger changes in energy between layers increases the amount of energy dissipated by charge carriers

thermally which decreases the maximum possible V_{OC} . Given the valence band edge for $\text{CH}_3\text{NH}_3\text{PbI}_3$, at 5.5 eV, an HTL material with a slightly reduced valence band edge is desirable. The valence band edge for CuI , at 5.1 eV, is reasonably positioned to serve this purpose. The valence band edge for Cu_2O , at 5.3 eV, appears to be an even better candidate based on this criteria alone.

The difference in conduction band edge between the intrinsic layer and the HTL is also of interest because, as stated earlier, a large conduction band offset acts as a barrier to electrons. The conduction band edge for CuI , at 2.0 eV, is offset significantly from that of $\text{CH}_3\text{NH}_3\text{PbI}_3$, at 3.9 eV, making it ideal as an electron barrier. The conduction band edge for Cu_2O , at 3.2 eV, is also appropriately positioned for this purpose, though the offset is not as large.

Of note is that similar band edge criteria could be applied to the ETL as it pertains to electron transport. The materials chosen as the ETL in this work were already validated for this purpose. The ETL was not, however, a focus of this research and was thus not optimized nor explored further.

With the theoretical and experimental background firmly established, the goals and motivations for this work should now be clear. Keeping these concepts in mind, it is now time to study the architecture and fabrication of the real $\text{CH}_3\text{NH}_3\text{PbI}_3$ solar cells produced. Once this has been covered, these devices and the Cu-based HTLs produced will be analyzed using a variety of material and electrical characterization techniques. Then, the proposed goals can be appropriately evaluated to see if they have been achieved.

III. DEVICE FABRICATION

Device Architecture

The devices produced for this work are inverted planar heterojunction organic perovskite photovoltaic cells. The device architecture is composed of glass/ITO/Cu-based HTL/ $\text{CH}_3\text{NH}_3\text{PbI}_3$ / C_{60} /BCP/Al layers where the Cu-based HTL is either CuI or Cu_2O . The band diagrams for each of these architectures can be seen in Figures 12a and c respectively. Additionally, the device architectures, with the layer thicknesses drawn to scale, can be seen in Figures 12b and d respectively. The ITO is pre-deposited on 1 inch square silicate glass slides with an appropriate pattern to fit 4 device die per slide. This pattern can be seen in Figure 13.

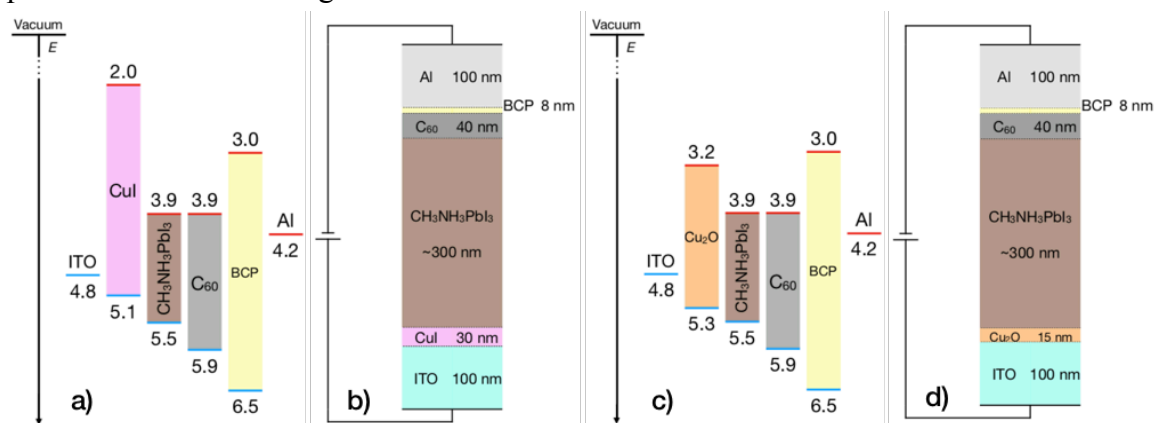


Figure 12: The a) architecture and b) band diagram of a $\text{CH}_3\text{NH}_3\text{PbI}_3$ perovskite solar cell device with a CuI HTL with the same c) and d) respectively for a device with a Cu_2O HTL. Valence band is in blue and conduction band is in red.

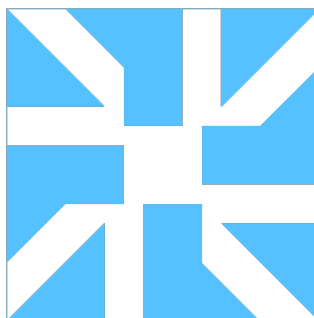


Figure 13: ITO (in blue) anode pattern printed on glass to fit 4 devices per slide.

Device Fabrication Process

The glass/ITO substrates were cleaned by sonication in a deionized (DI) water and detergent solution followed by a second sonication rinse in DI water only. The substrates were then dried with a carbon dioxide (CO₂) gas gun and the remaining water baked off on a hot plate at 105° C. A final plasma cleaning process was then performed to remove any organic residue. CuI spin coating solution was then prepared by dissolving solid CuI powder in acetonitrile at room-temperature. Several concentrations between 10 and 40 mg/ml were used in different device batches so that HTL thicknesses and device performance could be compared. All such solutions were filtered through a 0.2 μm polytetrafluoroethylene (PTFE) membrane syringe filter. 100 μl of the filtered solution was then spin coated on the cleaned glass/ITO substrates at 2000 to 4000 rotations per minute (RPMs) for 60 seconds. The CuI thin films were annealed at 150 °C for 10 to 20 minutes to improve crystallinity. All CuI layer processing was performed in a dry nitrogen (N₂) glovebox with both moisture and oxygen levels below 0.1 parts per million (PPM).

For devices made with a Cu₂O HTL, CuI thin films were converted to Cu₂O by submerging the completed glass/ITO/CuI slides in a sodium hydroxide (NaOH) solution at a concentration of 10 mg/ml in DI water. Slides were submerged for 10 to 30 seconds during which time the purple CuI film changed to a yellow color. The chemical reaction that occurs during the CuI to Cu₂O transition can be seen in Equation 11. After removing the slides from the NaOH solution, they were rinsed in DI water for 20 seconds to wash away any sodium iodide (NaI) residue, then dried using CO₂ and placed on a hot plate at



105 °C to drive off any remaining water. When desired, the resulting Cu₂O films were annealed at 250 °C or 350 °C for 1 hour to produce intermediate Cu₂O and CuO phases.⁵³ Note again that the CuO HTLs were never incorporated in completed solar cell devices and were only used for further HTL characterization. The full Cu-based layer fabrication procedure is illustrated in Figure 14.

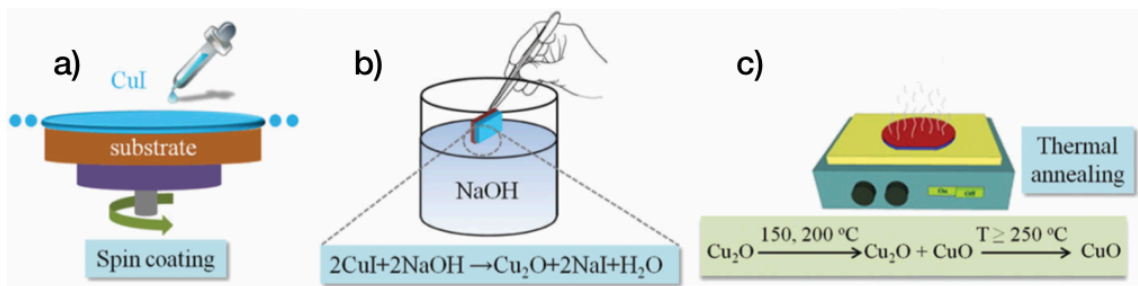


Figure 14: The Cu-based HTL fabrication process showing the a) spin coating, b) NaOH dip, and c) thermal annealing steps. Note that CuI annealing (at 150 °C), which would occur after spin coating, is not shown.⁵³

In order to optimize the HTL fabrication process, easily controlled process parameters were varied, one at a time, to find values that produced the best quality HTL as well as the best performing photovoltaic devices. In particular, a range of precursor solution concentrations and HTL spin coating RPMs were tried. At concentrations of 20 mg/ml or less, device PCE was found to be diminished from peak values with greater deviation between devices. At concentrations of 35 mg/ml or more, a similar but less pronounced trend was observed. When varying HTL spin coating RPMs, frequencies of 1500 or fewer RPMs were found to produce thin films lacking in thickness uniformity which resulted in devices with less than optimum PCE. At frequencies of 2500 RPMs or greater, the resulting thin films were found to be so thin (5 nm or less) that they no longer acted effectively as HTLs, resulting in devices with severely deficient and highly variable

PCEs. Other process parameters, such as CuI annealing time and NaOH dip time were found to have little impact on HTL quality and device performance. In total, the optimum HTL process parameters were found to be 30 mg/ml precursor solution concentration, 2000 RPMs spin coating, CuI annealing at 150 °C for 15 minutes, and dipped for 15 seconds in aqueous NaOH solution when converting to Cu₂O.

HTL stability was also explored by storing glass/ITO/CuI, glass/ITO/Cu₂O, and glass/ITO/PEDOT:PSS substrates for extended periods of time before incorporating them into complete photovoltaic devices. Samples stored for this purpose were kept in both normal atmosphere and dry N₂ environments for up to three weeks. For Cu-based HTLs, no significant difference in performance (principally PCE) values was observed between devices made with new HTLs versus devices made with weeks old HTLs. Furthermore, no significant difference was observed between Cu-based HTLs stored in atmosphere versus those stored in dry N₂. PEDOT:PSS HTLs, on the other hand, were found to degrade quickly, resulting in failed devices if used more than a few hours after initial HTL deposition. These results proved useful to device fabrication logistics because it permitted Cu-based HTLs to be prepared days in advance of the perovskite ink that must be promptly deposited after mixing.

A CH₃NH₃PbI₃ perovskite ink was mixed using a one step solution process using equal molar parts of lead iodide (PbI₂), methylammonium acetate (CH₃NH₃CH₃COOH), and methylammonium iodide (CH₃NH₃I) dissolved in dimethylformamide (DMF) at a 1.0 M concentration. 100 µl of the ink solution was then deposited on top of the Cu-based HTL by spin coating at 3000 RPMs for 60 seconds. All ink processing occurred in a dry

N₂ glovebox.

The glass/ITO/Cu-based HTL/CH₃NH₃PbI₃ structure was then annealed on a hot plate in atmosphere at 30 - 40 % humidity for 5 minutes to produce a high quality, polycrystalline perovskite film. Oddly, annealing the perovskite in atmosphere proved to produce better crystallinity than if annealed in dry N₂.³⁶ Using a pattern mask designed for the 4 device per slide architecture, some of the HTL and perovskite layers were then scraped off to prepare the devices for ETL deposition. The scraped slides were dusted off using dry CO₂, then loaded into a thermal evaporator inside an N₂ glovebox.

Approximately 40 nm of C₆₀ and 8 nm of bathocuproine (BCP) were deposited over the device area via thermal evaporation to act as the ETL. Although BCP has a band structure that does not initially seem to fit with the rest of the intended device architecture, experimental results have shown photovoltaic device performance improvement when it is coupled with a conductive material to form the ETL. The proposed mechanism behind this is that a thin layer of BCP reduces undesirable band bending that would otherwise occurs when an ETL is interfaced directly with a metal cathode.⁵⁴

100 nm of Al was then evaporated in an appropriate pattern over the device area to act as the cathode. The completed devices were then removed from the evaporator and loaded into an encapsulation printer which sealed the devices in an N₂ environment using a UV cured epoxy resin. The final encapsulated devices were removed from the N₂ glovebox and applied with Ag paint appropriately so they could be characterized by a solar simulator and multimeter apparatus.

IV. HTL MATERIAL CHARACTERIZATION

Atomic Force Microscopy

Atomic force microscopy (AFM) is an ultra-high resolution type of scanning probe microscopy (SPM) that employs a probe tip element in close contact with a sample surface to produce 3D topographical images. It is also capable of measuring minute atomic forces (as small as 10^{-18} N) as well as electrostatic potentials across a sample depending on the measurement configuration and probe type used. AFM combines the raster scanning principle of SPM with the probe tip principle of a stylus profilometer to achieve a measurement technique that is non-destructive to the sample. This is made possible by a highly sensitive piezoelectric cantilever system that oscillates the probe tip in such a way that it “taps” the surface of the sample without making direct contact. The tip’s interaction with the surface causes it to be deflected by the sample’s topographical features. These deflections are then recorded by the cantilever as the probe scans and the collected data is compiled to produce a 3D image. Due to the nanoscale precision of the probe tip, lateral features as small as 30 Å and vertical features as shallow as 1 Å can be imaged. Furthermore, since no particle beams or electromagnetic field configurations are required to produce the image, AFM can generally be performed in atmosphere and without a need to consider material properties such as conductivity or optical transparency. These aspects make AFM measurements attractive when analyzing delicate samples that may be compromised by other types of microscopy.⁵⁵

In this work, the basic tapping mode of AFM is used to measure the surface roughness and to image the morphology of CuI, Cu₂O, and CuO HTLs. AFM images

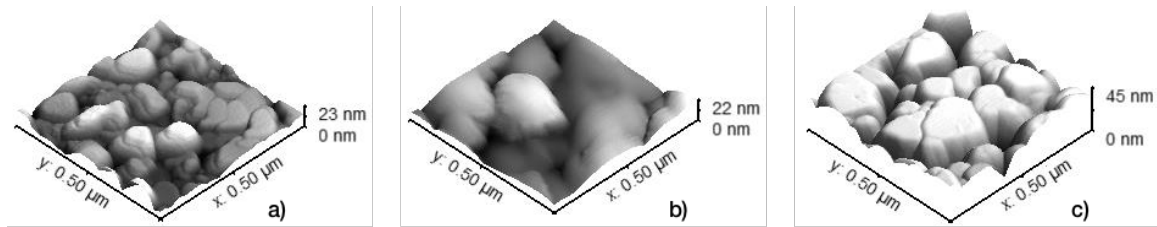


Figure 15: AFM images of CuI HTLs deposited at a) 30, b) 20, and c) 10 mg/ml precursor solution concentrations.

were taken to compare CuI HTLs made with 10, 20, and 30 mg/ml CuI in acetonitrile precursor solution concentrations. These images can be seen in Figure 15. AFM images were also taken to compare Cu₂O and CuO HTLs made with optimized process parameters. These images can be seen in Figure 16. The lateral plane of all images taken was a 500 nm square.

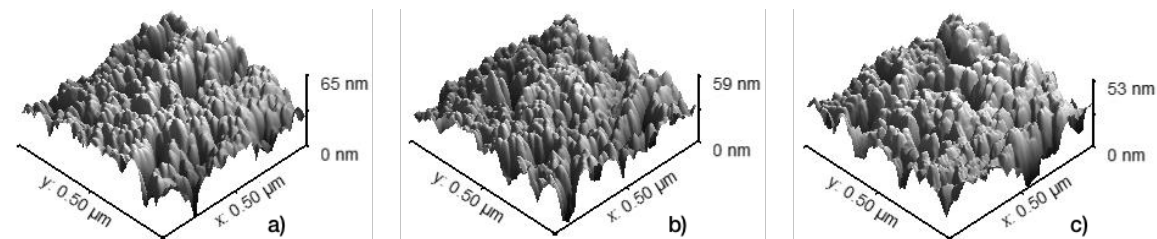


Figure 16: AFM images of copper oxide HTLs processed from CuI including a) Cu₂O, b) CuO (250 °C annealing), and c) CuO (350 °C annealing) samples.

The maximum vertical displacement, R_{max} , for the different HTL sample groups ranged from approximately 20 to 65 nm while root mean square roughness, R_q , values ranged from 3.9 to 9.5 nm. R_{max} and R_q values can be seen for each sample type in the bar graphs shown in Figures 17a and b respectively. 10 and 20 mg/ml CuI samples lacked coherent grain structure and therefore had nearly equal roughnesses of 4.0 and 3.9 nm respectively. 30 mg/ml CuI samples showed a clear grain structure with tightly packed grains ranging from 100 to 300 nm across. Due to some visible gaps between grains, the 30 mg/ml CuI had a higher roughness of 6.5 nm as is expected for a large grain

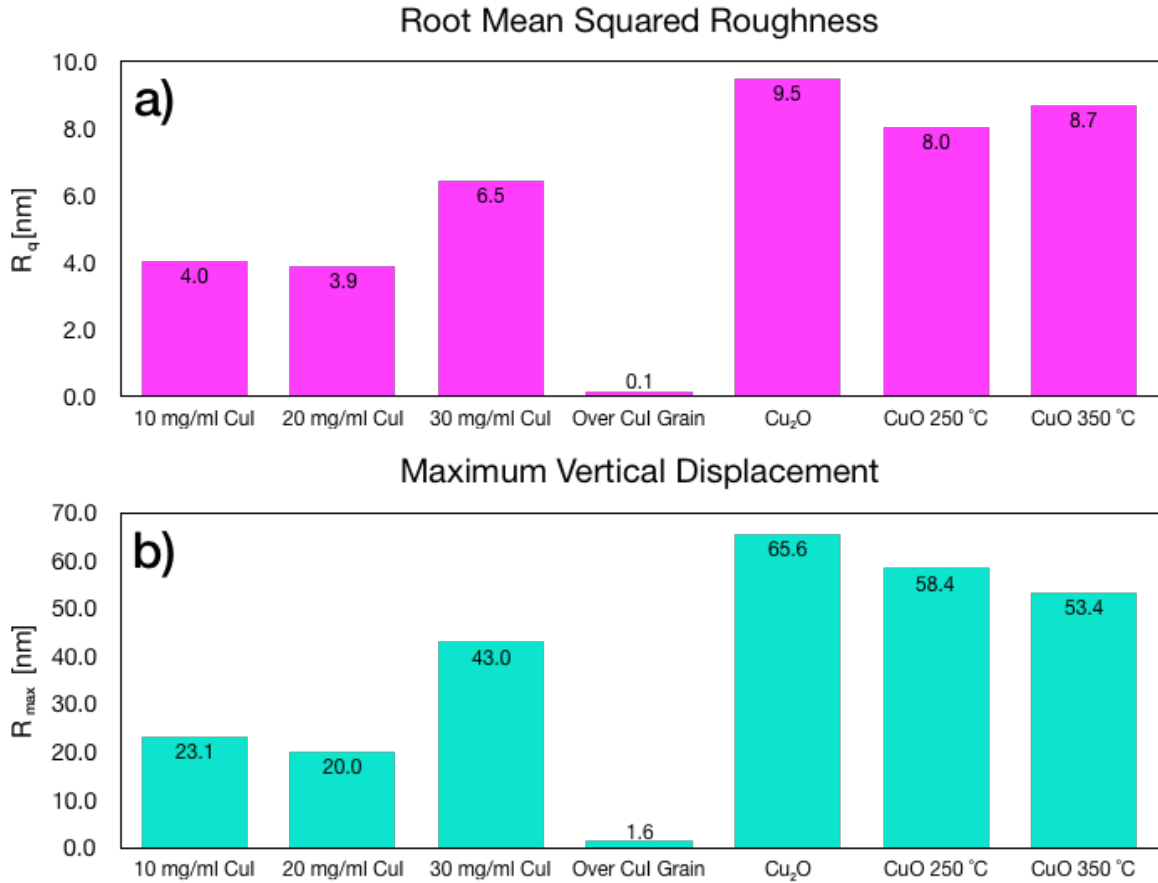


Figure 17: Bar graphs of a) root mean square roughness, and b) maximum vertical displacement measured by AFM.

polycrystalline thin film. As a side note, when calculating R_q on an area restricted to just the flat plateau of a large CuI crystal grain, the result is routinely less than 0.1 nm indicating a highly ordered structure within a single grain. This result was further supported by x-ray diffraction data, shown in a later section.

Cu_2O and CuO samples all showed a random and rough popcorn-like texture regardless of annealing temperature. Examining the AFM images alone, it was impossible to differentiate the copper oxide HTLs. R_q values indicated roughnesses between 8.0 and 9.5 nm with CuO samples generally showing slightly less roughness than Cu_2O samples. These results seem to indicate that all copper oxide samples are neither Cu_2O nor CuO,

but rather some intermediate and amorphous Cu_xO phase. Furthermore, this also seems to indicate there is little difference between Cu_xO samples regardless of whether an annealing step is used after the NaOH dip process or not. This outcome would be further corroborated by other characterization techniques.

Stylus Profilometry

Stylus profilometry is a surface characterization technique that operates by scanning a mechanical stylus apparatus across a sample to produce a topographical profile.⁵⁶ It is most commonly used to measure the roughness and thickness of a specimen's exterior features. While there does exist non-contact varieties of profilometry, typical stylus profilometry requires a probe tip to directly contact the sample surface, thus making it a potentially destructive measurement technique.⁵⁷ A schematic diagram of a simple stylus profilometer measurement setup is shown in Figure 18.

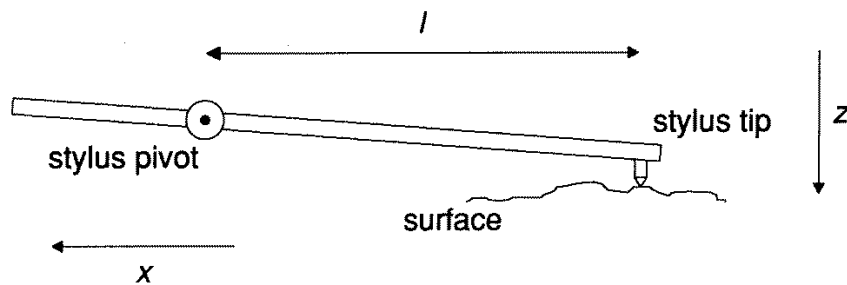


Figure 18: A schematic diagram of a stylus profilometer measurement setup along length l , with scan axis, x , and displacement axis, z .⁵⁶

For this research, stylus profilometry was used to determine the thickness of Cu-based HTLs and to corroborate the vertical scale measured by AFM. Due to the error in vertical resolution of the profilometry tool used, which is about 2 nm, HTLs measured to be 8 nm or thinner should be treated with scrutiny. CuI, Cu_2O , and CuO HTLs made from

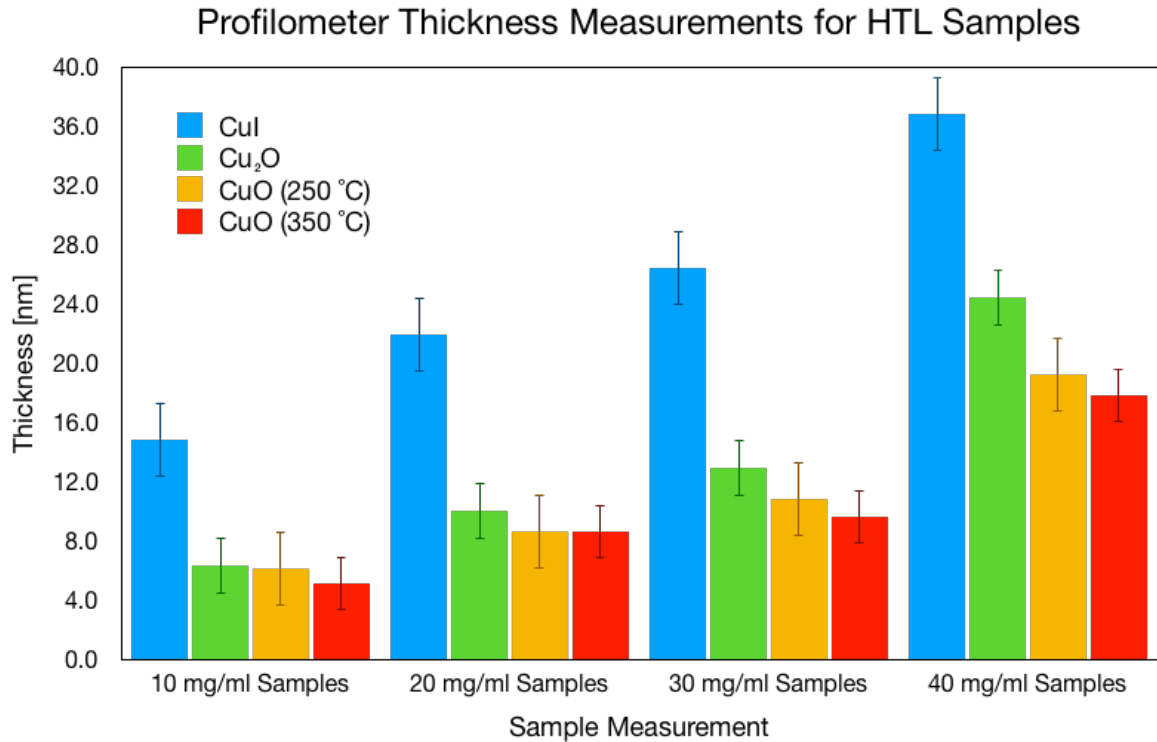


Figure 19: Profilometer results showing averages for CuI, Cu₂O, and CuO samples of different thicknesses controlled by precursor solution concentration.

10, 20, 30, and 40 mg/ml CuI in acetonitrile precursor solution spun at 2000 RPMs were included in the sample population for this metrology method. The average thicknesses for these samples are shown in Figure 19 with error bars indicating the deviation in measurements for each sample type. The deviations for each sample type were in close agreement with the approximately 2 nm error expected from the tool. It should be noted that for copper oxide samples, R_q values from AFM indicate a roughness of 74 to 90% of the total thickness measured by profilometry. This brings the uniformity of copper oxide thin films into doubt and further enforces the 8 nm minimum thickness cutoff for profilometer measurements.

When examining the thickness results for each of the HTL sample types, a particular trend dependent on the precursor solution concentration was observed when

fixing the spin coating speed to 2000 RPMs. This trend proved useful in consistently estimating the HTL thickness for a given Cu-based material. The specifics of this trend will be given for each of the HTL sample types listed above and are calculated from values shown in Figure 19.

For CuI samples, the thicknesses were found to have a nearly linear relationship with precursor solution concentration at a rate of 0.9–1.5 nm per mg/ml. This rate was higher for 10 mg/ml CuI samples but stabilized to near 1.0 nm per mg/ml for 20, 30, and 40 mg/ml samples. A similar trend would also hold true for the other Cu-based HTLs provided all fabrication parameters other than precursor solution concentration were held constant.

For Cu₂O samples, a rather sizable amount of thickness was found to be lost when converting the sample from CuI to Cu₂O via the NaOH dip process. The reason for this loss is likely due to the difference in size between the CuI lattice constant of 6.1 Å and the Cu₂O lattice constant of 4.3 Å, which is a predicted loss of about 30%. The loss in thickness measured by profilometry ranged from a high of 57% in 10 mg/ml samples to a low of 34% in 40 mg/ml samples. The resulting Cu₂O thicknesses were found to be related to the precursor solution concentration at a rate of 0.43–0.63 nm per mg/ml.

For CuO samples, a much smaller amount of thickness was found to be lost when converting the samples from Cu₂O to CuO via the thermal annealing process. In general, CuO samples annealed at 250 °C showed a slightly smaller thickness loss than those annealed at 350 °C. The 250 °C annealed sample thickness losses ranged from a high of 21% in 40 mg/ml samples to a low of 3% in 10 mg/ml samples. The 350 °C annealed

sample thickness losses ranged from a high of 27% in 40 mg/ml samples to a low of 14% in 20 mg/ml samples. The resulting CuO thicknesses were found to be related to the precursor solution concentration at a rate of 0.36–0.61 nm per mg/ml for 250 °C annealed samples and a rate of 0.32–0.51 nm per mg/ml for 350 °C annealed samples.

Scanning Electron Microscopy

Scanning electron microscopy (SEM) is an ultra-high resolution type of electron microscopy that is capable of producing images of greater than 300,000 times magnification.⁵⁸ This gives it an effective resolution approaching 1 nm, making it possible to capture images of features close to the electron tunneling limit. Such an incredible resolution is made possible because electrons have wavelengths much shorter than the optical diffraction limit of approximately 250 nm. Thus, SEM is a popular imaging technology for probing features smaller than those accessible by optical microscopy.⁵⁹ Furthermore, as electrons have unique quantum interactions with different chemical elements, most SEMs also include additional detectors that allow for materials characterization beyond simple imaging.⁶⁰ One such technique was used in this research and will be discussed in the next section.

The SEM operates by raster scanning an electron beam across a sample and detecting the signal produced by the interaction between the beam and the specimen. Just like optical microscopy, SEM also makes use of lenses to focus and control the beam that composes the image. However, where an optical microscope uses a series of physical glass lenses to achieve the desired magnification effect, an SEM uses lenses formed by

concentrated electromagnetic fields.⁵⁸ A basic conceptual diagram of an SEM electromagnetic lens can be seen in Figure 20a while a schematic diagram of two types of SEM lens configurations can be seen in Figures 20b and c. The SEM used in this research had a semi in-lens objective with additional detectors permitting other characterization techniques.

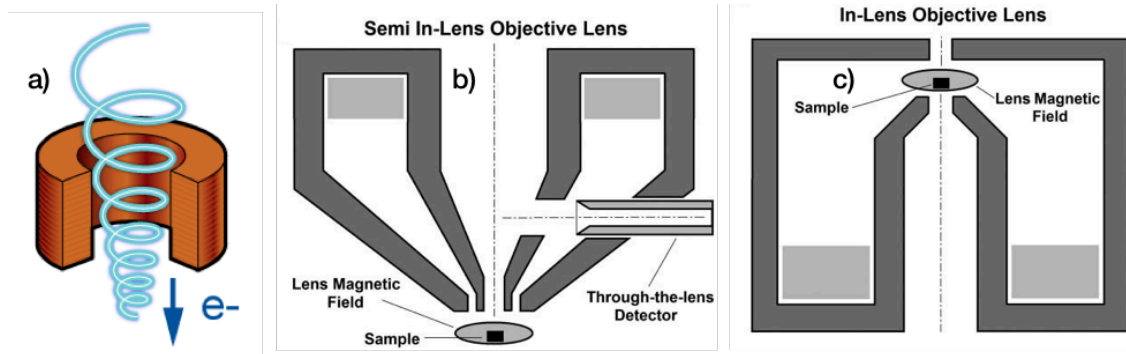


Figure 20: Schematic diagrams of a) conceptual, b) semi-in-lens objective, and c) in-lens objective SEM lens arrangements.^{58, 60}

In this work, SEM was used to take planar images to determine the morphology of CuI, Cu₂O, and CuO HTLs. These images also served to corroborate the previously discussed AFM morphology results. Additionally, a cross-sectional image was taken of the layer stack of a completed device so that relative layer thicknesses and interface transitions can be seen. This cross section is shown in Figure 21. It should be noted that the cross-section area was cut via focused ion beam (FIB) on a stage of non-orthogonal tilt, so some layers may appear thicker than they actually are in operational devices.

The planar images of HTL samples can be seen in Figure 22. All four sample images have the same magnification and thus the same image dimensions, which is about 3 μm square for each image. Furthermore, all four images are of HTL samples fabricated with optimized process parameters.

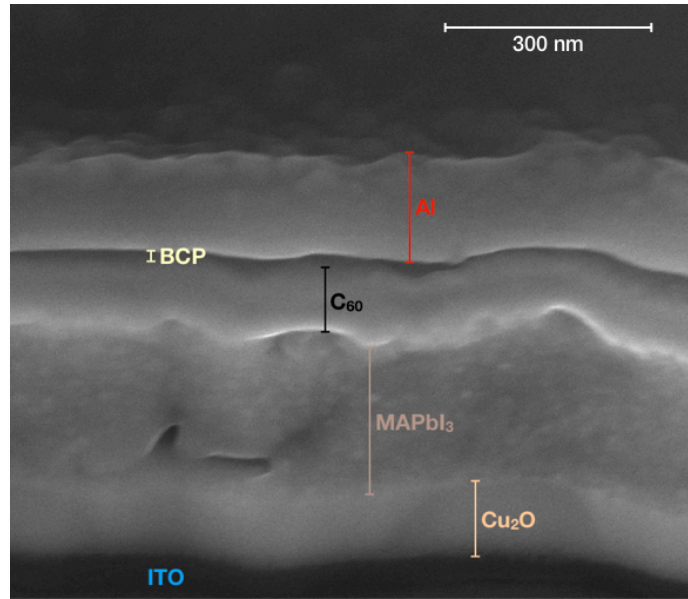


Figure 21: SEM cross-section image of a completed device with a Cu₂O HTL showing all layers. Note that the ITO/Cu₂O interface may not be visible.

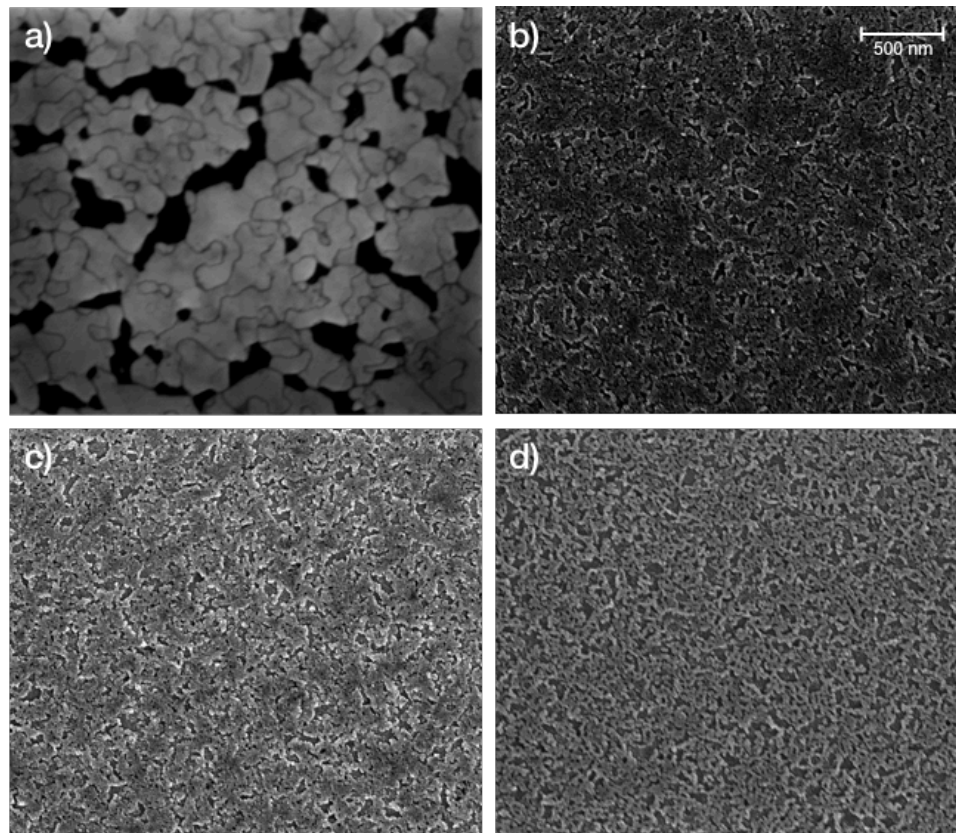


Figure 22: Planar SEM images of a) CuI, b) Cu₂O, c) CuO (250 °C annealing), and d) CuO (350 °C annealing) HTL samples. Each sample type was found to be roughly isotropic, producing similar features everywhere along the HTL surface.

Although only a single image for each sample type is shown here, a multitude of images collected for each sample indicated that each HTL was roughly isotropic across the entire sample surface. Thus, the images provided here serve as a reasonable example of the morphology for each HTL type. The planar image of the CuI HTL shows a clear polycrystalline grain structure with most grains being between 200 and 400 nm long with some small gaps in-between that are never wider than about 100 nm. This compared well with the 30 mg/ml CuI samples analyzed previously under AFM results. The Cu₂O and CuO samples, however, all have a rough and randomly textured appearance. This outcome agrees with the potentially amorphous morphology results already indicated by AFM images of copper oxide samples.

If indeed the Cu₂O and CuO samples are amorphous, this would indicate that neither compound is actually present and that some intermediate Cu_xO phase dominates, a possibility already discussed earlier. Such a result could be further validated by measuring atomic ratios via energy dispersive x-ray spectroscopy and effectively proven by x-ray diffraction techniques. These characterization methods were both performed for this research and will be discussed in subsequent sections.

Energy Dispersive X-Ray Spectroscopy

Energy dispersive x-ray spectroscopy (EDS) is a spectroscopic analysis technique that reveals elemental composition by measuring the x-rays emitted from a sample bombarded by a particle beam. Since the electron beam used in an SEM is of sufficient energy to produce x-ray backscatter after colliding with a specimen, EDS is a commonly

included characterization method offered in such analysis equipment. As each atomic element has a unique x-ray emission spectrum, both identification and stoichiometric relations of constituent elements in a material can be determined by EDS. Because of this, EDS analysis is often used in conjunction with SEM images to definitively prove the presence of elements already suspected to exist in a sample. It should be noted, however, that while EDS is great at measuring atomic ratios, it cannot extrapolate the molecular identity of the compounds measured. EDS is thus most useful in addition to other characterization techniques or existing knowledge of a familiar sample.⁶¹

For purposes of this research, EDS was performed on each of the Cu-based HTLs to corroborate their suspected elemental composition. The penetration depth of the EDS characterization tool was on the order of 1 μm meaning that the HTL, anode, and substrate glass would appear in the spectroscopy results. As the anticipated stoichiometry of CuI, Cu₂O, CuO, ITO, and silicate glass are easily deduced, numerical models of the predicted results were constructed before EDS measurements were taken. These models were then compared to the actual measurements to show that the glass/ITO/Cu-based HTL samples had the expected atomic make-up. This comparison proved to be successful overall, but did have one notable discrepancy that potentially indicated an amorphous morphology to the copper oxide thin films produced.

The comparison of measured EDS results to model predictions is shown in Figure 23. The models used for comparison considered any compounds that could be present in the glass/ITO/Cu-based HTL structure as well as any compounds from contamination that could occur during processing CuI into some kind of copper oxide. The original model

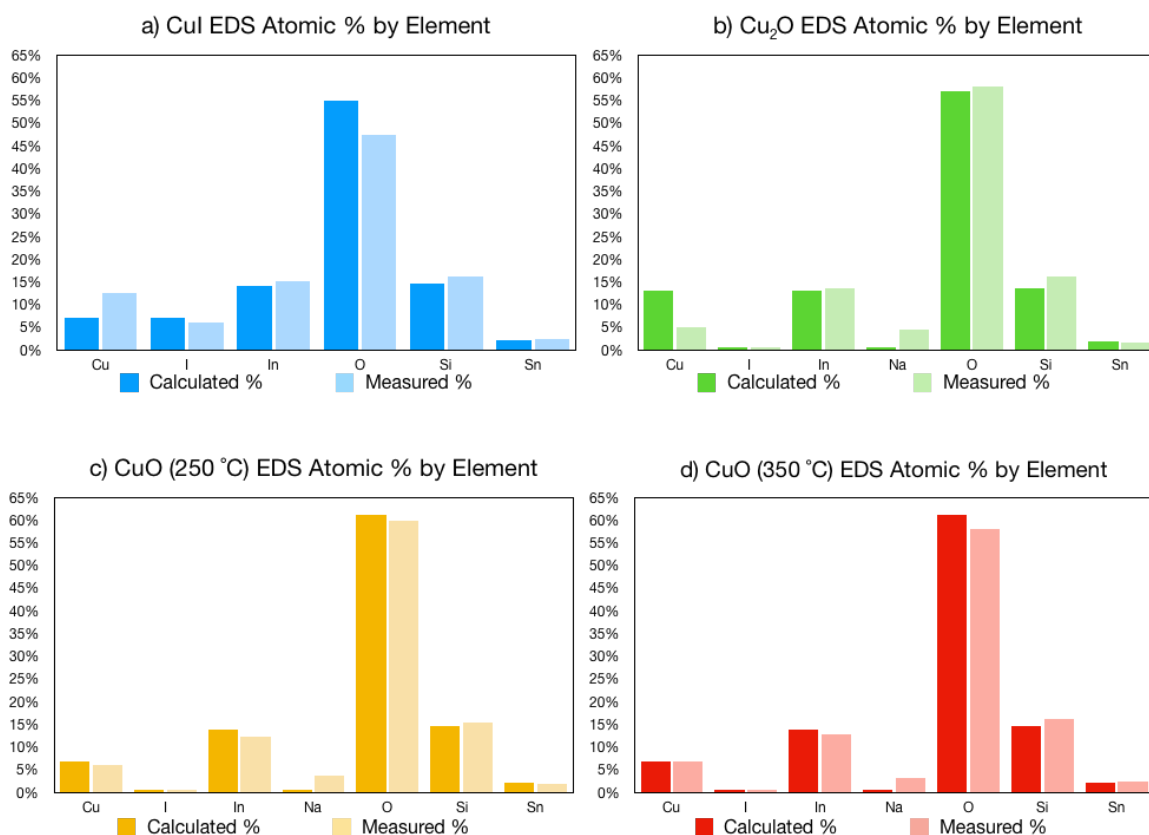


Figure 23: Comparison of EDS measured vs calculated atomic percentage results for a) CuI, b) Cu₂O, and c) 250 °C and d) 350 °C annealed CuO samples.

consisted of 2 parts SiO₂, 1 part ITO (which is 0.8 parts In₂O₃ and 0.2 parts Sn₂O), 1 part of a Cu-based HTL compound (either CuI, Cu₂O, or CuO), and 0.1 parts NaI to account for contamination during the NaOH dip process. After a few initial measurements of substrates, a more accurate model was tailored to consist of 2.1 parts SiO₂, 1.3 part ITO (which is 1.0 parts In₂O₃ and 0.3 parts Sn₂O), 1 part of a Cu-based HTL compound (either CuI, Cu₂O, or CuO), and 0.1 parts NaI. It was later found that the glass substrates had a small percentage of Na without any other counter component indicating the glass was a variety of soda glass. This was not taken into account for the model and did not significantly impact predicted results.

In general, measured EDS results matched with the expected atomic percentages

closely. There was possible discrepancy in the predicted amount of copper in the initial CuI HTLs, but as it showed an over abundance of Cu, this was not expected to negatively affect HTLs being further processed in some form of copper oxide. However, the Cu percentage measured for the supposed Cu₂O samples did show a significant under abundance of Cu that matched the expected results for CuO much more closely than those expected for Cu₂O. This was found to be true for several Cu₂O samples and seems to indicate that whatever Cu_xO phase is actually present has a content much higher in CuO than Cu₂O regardless of whether or not the NaOH dip process is followed by thermal annealing. This further supports the body of evidence suggesting that the copper oxide films prepared for this work are amorphous. The final piece of evidence to confirm this will be discussed in a later section covering x-ray diffraction.

Ultraviolet-Visible Spectroscopy

Ultraviolet-Visible Spectroscopy (UV-Vis) is a type of spectral characterization method capable of determining a material's identity, band gap, and molecular structure. It operates by passing a monochromatic beam through a sample to produce an absorbance, reflectance, and/or transmission spectrum based on the amount of light that reaches the photodetector on the other side. As is suggested by the technique's name, UV-Vis uses a light source and monochromator to produce a beam that can range in wavelength from the ultraviolet to the near-infrared. The general experimental setup, shown in Figure 24, commonly includes a reference and test sample so that undesired contributions to the spectra from certain sample layers (such as a glass substrate) can be subtracted out.⁶²

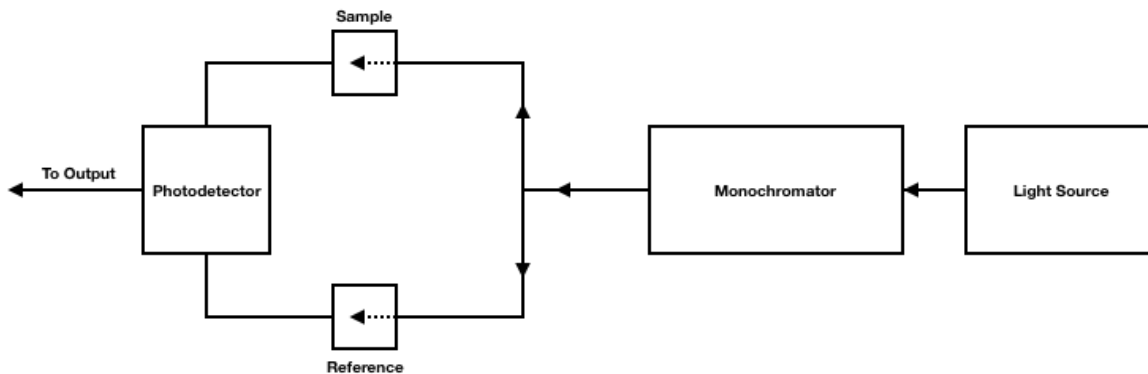


Figure 24: Schematic diagram of UV-Vis experimental setup showing all equipment components.

As adapted for thin films, UV-Vis is often used to collect transmission spectra, which are invaluable tools for characterizing transparent and semi-transparent materials found in optical applications. Absorbance spectra is also commonly taken to roughly determine a thin film's band gap. This characterization is especially useful for the component layers of a solar cell, where appropriate band gap with high transmittance and low reflectivity is required in order to maximize device performance.

Although this work does not employ UV-Vis to probe molecular structure, it does compare the measured transmission spectra to those of known samples from current literature. Absorbance data was also taken to determine the approximate band gap of the different HTLs and compared these to expected values from literature. ITO, CuI, Cu₂O, CuO, and PEDOT:PSS samples were analyzed and compared for their transmission spectra and CuI, Cu₂O, and CuO HTL samples were analyzed for their absorbance spectra. All samples were measured over a spectral range of 200 to 900 nm. Furthermore, all HTL samples were fabricated using optimized process parameters.

The transmission spectra for the various sample types can be seen in Figure 25.

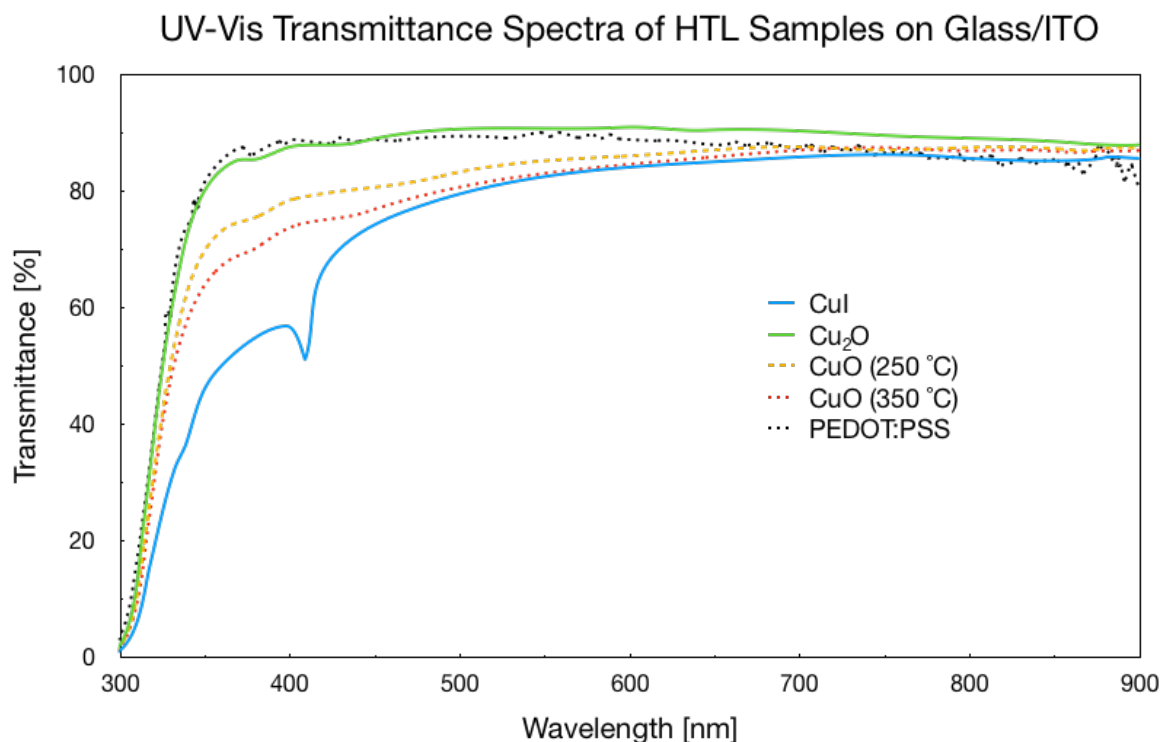


Figure 25: UV-Vis transmittance data for CuI, Cu₂O, CuO, and PEDOT:PSS HTL samples deposited on glass/ITO.

Notice that there are clearly defined characteristic creases in the spectra for a CuI HTL. These occur at approximately 410 and 350 nm and are a clear indication of γ -CuI with a preferred (111) orientation.^{53, 63–66} Optical transmittance above 450 nm is approximately 80% for CuI samples. Cu₂O and PEDOT:PSS samples maintain an optical transmittance approaching 90% until about 360 nm at which point it rapidly decreases. The trend for CuO transmittance also closely matches that of Cu₂O and PEDOT:PSS but at a lower value of approximately 80%.

The absorbance spectra for the various HTL types can be seen in Figure 26.

Notice that there is a characteristic peak in the spectra for CuI HTLs at 410 nm, matching the location of the corresponding crease in the transmittance spectra. This peak indicates an absorption onset of about 423 nm, which is equivalent to a band gap of 2.93 eV. This

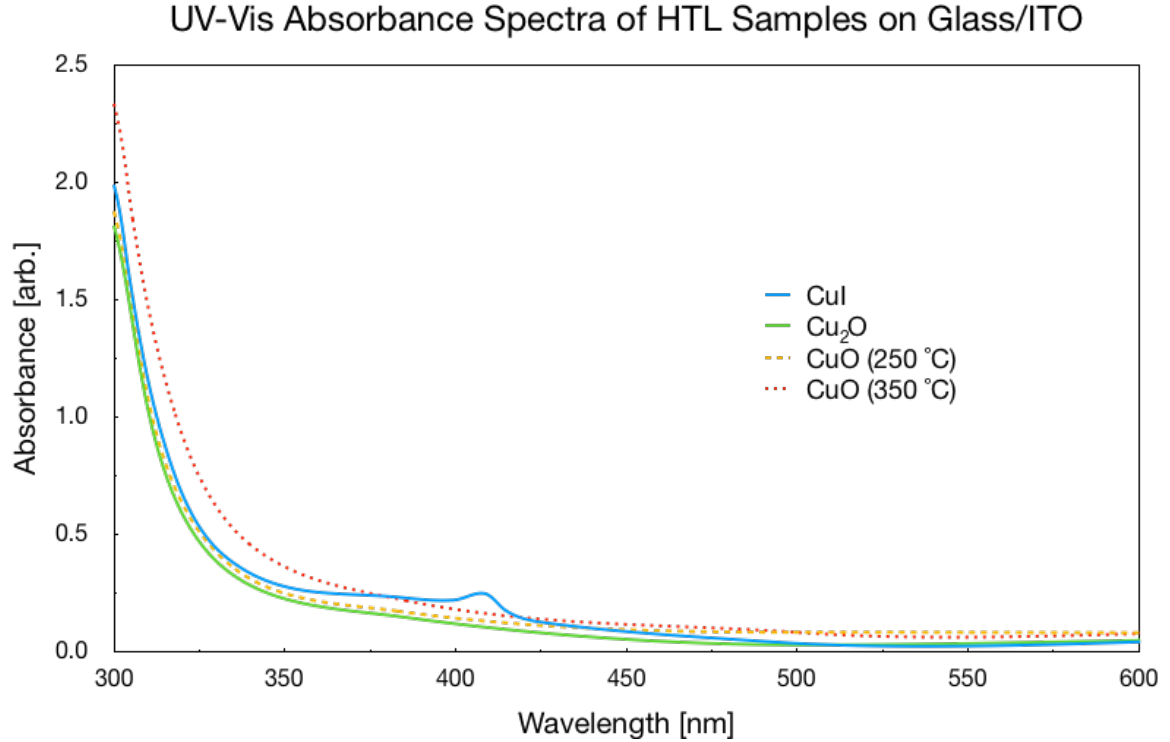


Figure 26: UV-Vis absorbance data for CuI, Cu₂O, and CuO HTL samples deposited on glass/ITO.

is nearly equal to the 2.96 eV reported for thin film γ -CuI from literature.⁶⁴

It should be noted here that while the presence of clear absorption peaks can suggest a crystalline morphology, not all crystalline materials reveal such peaks when optical absorbance is taken at room-temperature. This is because the formation of excitons occurs when the difference between the band gap and the photon energy approaches the exciton binding energy. If this binding energy is sufficiently larger than the thermal energy, kT , which is approximately 25.9 meV at room-temperature, then the absorption peak will be discernible. Otherwise, the peak will be washed out from the fundamental absorbance curve.¹⁵ Thus, the exciton binding energy of γ -CuI, which is approximately 58 meV,⁶⁷ is large enough to produce a clear absorption peak in the measured UV-Vis absorbance spectra.

The band gaps for the copper oxide HTLs proved more difficult to derive due to the lack of coherent absorption peaks. Instead, the point of a notable change in slope along the absorbance curve was used to roughly determine the onset of absorption and then calculate the equivalent band gap. This yielded band gaps of 2.60 eV for Cu₂O HTLs, 2.58 eV for CuO samples annealed at 250 °C, and 2.54 eV for CuO samples annealed at 350 °C. Each of these is significantly higher than the literature values for these compounds in bulk form which is generally 2.1 eV for single phase cubic Cu₂O⁴⁷ and 1.5 eV for single phase monoclinic CuO.⁴⁸ However, the higher band gap estimates for copper oxide HTLs are in close agreement to literature results for thin films of the same materials,⁶⁸ which will be used later for ellipsometry analysis.

X-Ray Diffraction Crystallography

X-Ray Diffraction Crystallography (XRD) is a material characterization technique that can determine the crystal structure, lattice orientation, degree of crystallinity, and other related properties of solids. The development of the physical theory behind XRD was a monumental achievement in the history of solid state physics that resulted in the 1915 Nobel Prize being awarded to crystallography pioneers William and Lawrence Bragg. They proposed that when x-rays penetrated a solid sample, the beam would be diffracted by the planes of the atomic lattice of the material. Based on the atomic spacing between planes, the intensity of scattered x-rays should peak where they constructively interfered. As predicted, this occurred when the phase shift of the x-rays was a multiple of 2π . Since the distance between planes in a lattice is uniquely determined by the type of

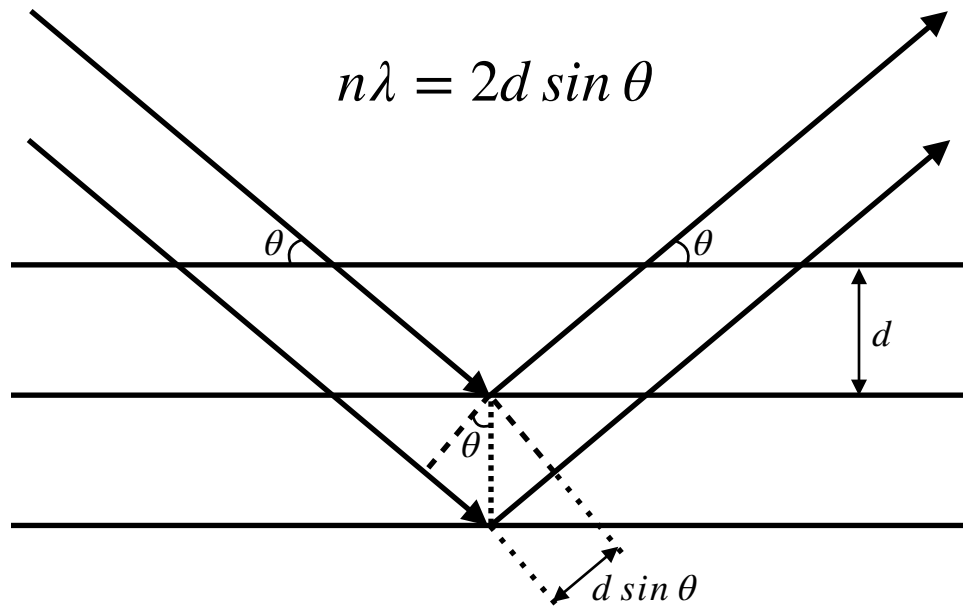


Figure 27: Geometric diagram of x-rays scattering off atomic planes causing diffraction according to Bragg's Law.

atomic bonding present, the angles at which these diffraction peaks appear can be used to determine the crystal composition, structure, and orientation of any well-ordered solid.

The geometric relationship that governs this process, now known as Bragg's Law, can be seen in Figure 27.⁶⁹

The XRD performed for this research was standard Bragg Diffraction which measures the intensity of diffracted x-rays against the diffraction angle, 2θ . CuI, Cu₂O, and CuO HTL samples fabricated with optimized process parameters were measured. The resulting XRD peak patterns were compared with those found in literature to determine the crystallographic phase and orientation of the HTL thin films.

CuI HTL samples showed clear diffraction peaks at approximately 26°, 53°, and 84°. From literature, these correspond to the (111), (222), and (333) planes respectively of γ -CuI⁶⁴⁻⁶⁶ that forms in the zinc blende structure when annealed at temperatures below 390 °C.⁴³ The XRD pattern for CuI can be seen in Figure 28 with the (111), (222), and

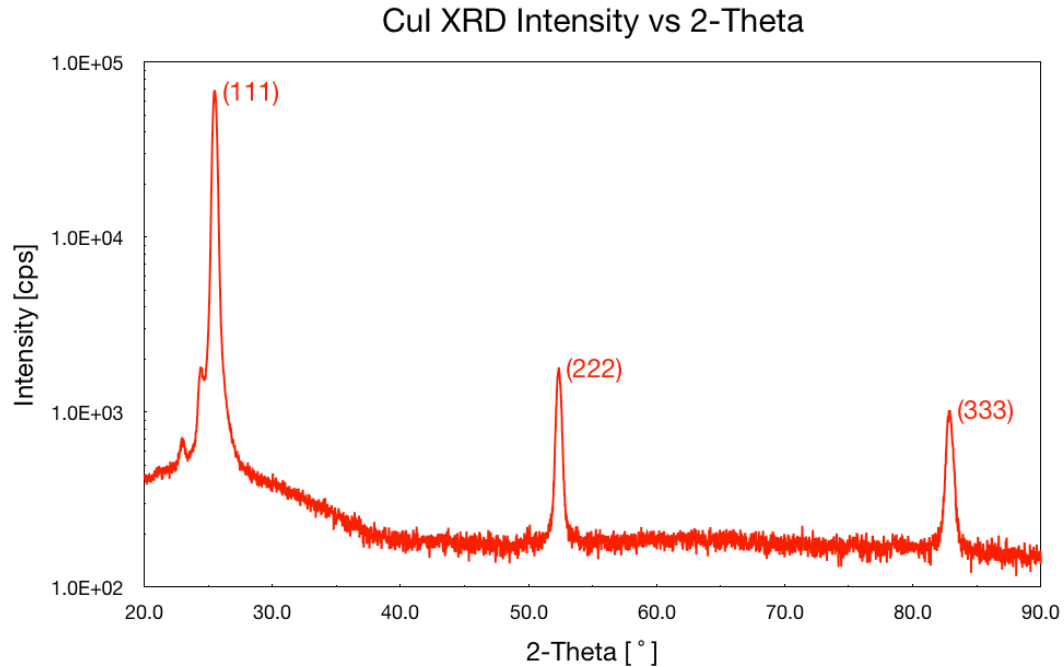


Figure 28: XRD pattern for a CuI HTL sample clearly showing the {111} family of planes, indicating strong γ -phase crystallinity.^{66, 68, 69} All such CuI HTL samples measured matched these results.

(333) peaks clearly marked.

Cu₂O and CuO HTL samples showed no discernible diffraction peaks despite considerable effort to produce samples in an environment that favored crystal nucleation. The same CuI to Cu₂O conversion NaOH dip process was used to create copper oxide on a variety of substrates, including highly ordered (100) silicon, as well as using a variety of in and out-of-atmosphere annealing methods at a variety of temperatures. Although the same process was claimed to produce weakly crystalline Cu₂O and CuO in literature,⁵³ no such crystallinity was ever observed in this study. The XRD pattern produced for all Cu₂O and CuO samples can be seen in Figure 29 showing only noise. This directly indicates amorphous morphology. As all other material characterization techniques agree with this assessment, it is reasonable to conclude that all copper oxide HTLs were an

amorphous phase of Cu_xO close in composition to CuO .

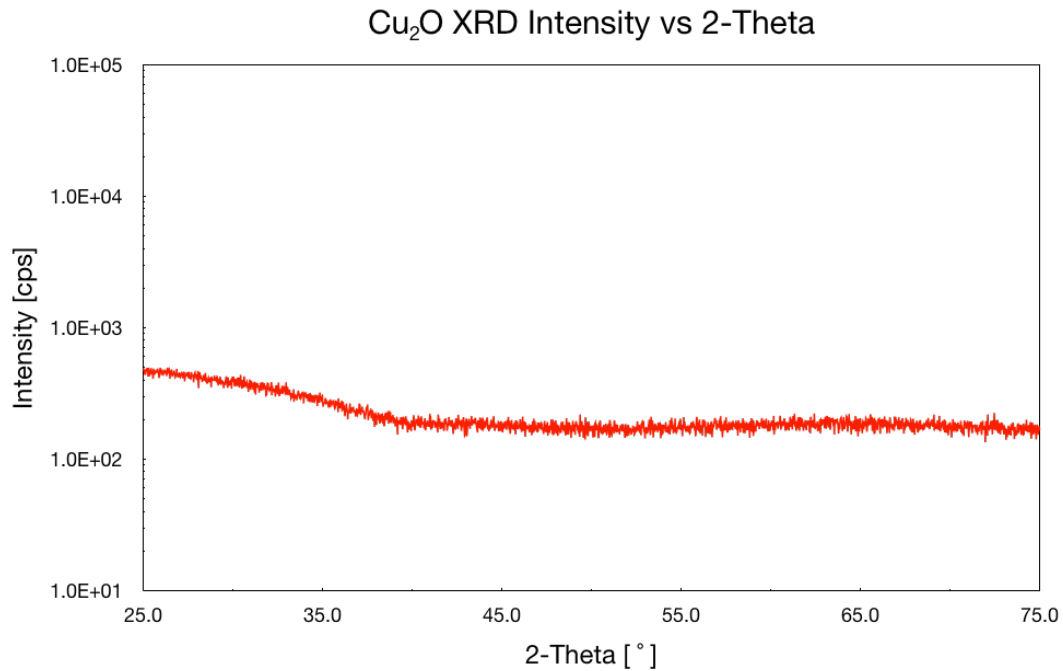


Figure 29: XRD pattern for a Cu_2O sample showing only noise, indicating amorphous morphology. All copper oxide HTL samples measured matched these results.

Spectroscopic Ellipsometry

Spectroscopic Ellipsometry (SE) is an optical characterization method used to determine a material's optical properties including refractive index, electric permittivity, and extinction coefficient. Although it can be used to analyze various forms of semiconductor materials, SE is most often used for thin films that range from optically opaque to semi-transparent. The basic principle of operation behind SE is that the polarization state of light changes after reflection off a material surface. An ellipsometer measures these changes and compares them to a model that predicts what these changes should be for an ideal sample of a known material. A schematic diagram of the SE

measurement setup can be seen in Figure 30.⁷⁰

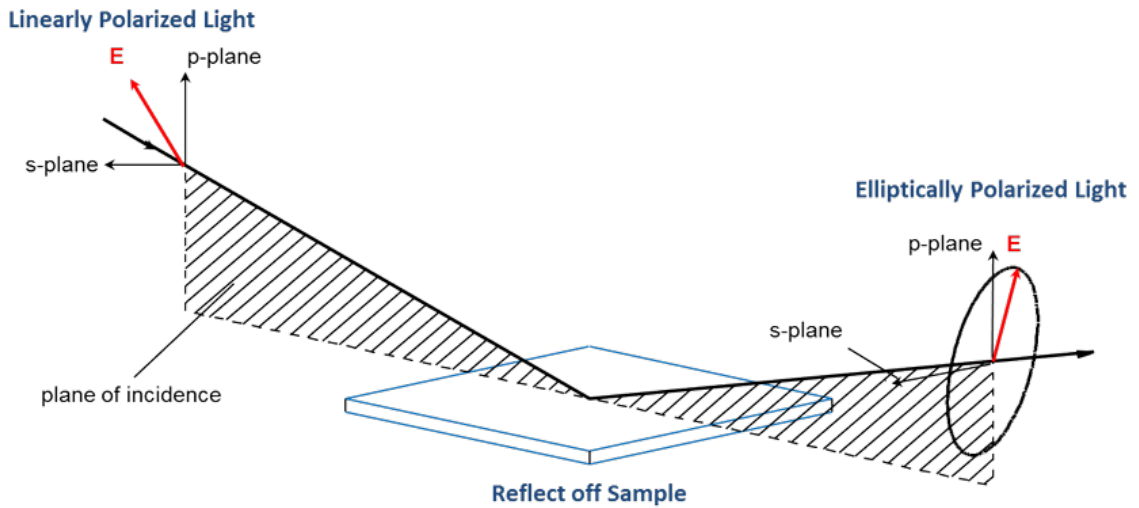


Figure 30: Schematic diagram of SE experimental setup showing polarization components and interaction with sample surface.⁷⁰

When specifically examining thin film specimens, SE can also resolve other useful parameters such as layer composition, thickness, and roughness. What is most remarkable about SE is that the wide array of material properties it can account for are all derived from a single measurement parameter, the complex reflectance ratio, ρ_r , which is most commonly defined by an amplitude component, Ψ , and a phase component, Δ , as shown in Equation 12.⁷¹ Such a simple relationship may make it tempting to think that

$$\rho_r = \tan(\Psi) e^{i\Delta} \quad (12)$$

the mathematical framework behind SE is easily understood. This is in error, however, as a wide array of mathematical tools are required to extract the desired characterization parameters from ρ_r . As a rigorous explanation of the physics behind SE is far beyond the scope of this work, only a few necessary equations will be presented here to expound upon how the ellipsometry models used for this research were derived and why they were chosen.

In this research, SE was used to determine the refractive index and extinction coefficient profiles of CuI, Cu₂O, and PEDOT:PSS HTLs as well as glass/ITO and bare glass substrates. HTLs of different thicknesses controlled by precursor solution concentrations were deposited on both glass/ITO and bare glass substrates. Additionally, to aid in the constructing of accurate models for each material, thickness data from profilometry and roughness data from AFM were incorporated into initial model parameters before model fitting algorithms were applied. SE measurements of the glass/ITO/HTL and glass/HTL sample groups were compared to help parse out the ITO and Cu₂O signals. This was necessary in order to form reliable models of refractive index and extinction coefficient for each oxide. As the SE signals for CuI and PEDOT:PSS are far more easily differentiated from substrate material signals, models for these materials were achieved without requiring this comparison. With the data and sample groups utilized for SE analysis now addressed, the mathematical techniques and motivations used to produce these models will now be briefly described.

The first steps in constructing a reliable and accurate SE model for any thin film is to already have a few known physical parameters about the material so the model has a reasonable starting point. For the models constructed here, this was thickness and roughness data. Also, UV-Vis data showed that all HTLs and substrate materials were consistently 75% or more optically transparent in the range of 450 to 900 nm. This is particularly useful for modeling thin film behavior in the visible range because it reveals that the extinction coefficient, k , in this range must be effectively zero. Such a condition is highly favorable for modeling refractive index, n , as a function of wavelength, λ , using

a Cauchy Equation, which is shown in Equation 13 to three terms. The coefficients a , b ,

$$n(\lambda) = a + \frac{b}{\lambda^2} + \frac{c}{\lambda^4} + \dots \quad (13)$$

and c were optimized by CompleteEASE software. As the value of each subsequent coefficient gets orders of magnitude smaller, only a was considered as the appropriate value for n once fitting was done. On the first pass, the known thickness and roughness values were provided, k was set to zero, and the coefficients were optimized by a non-linear fitting procedure until best fitting values were found.

To quantify the accuracy of all models, a goodness of fit parameter, the mean square error (MSE), shown in Equation 14, was used. This equation includes the number

$$MSE = 1000 \sqrt{\left(\frac{1}{3m - 1}\right) \sum_{i=1}^m [(N_{E_i} - N_{G_i})^2 + (C_{E_i} - C_{G_i})^2 + (S_{E_i} - S_{G_i})^2]} \quad (14)$$

of wavelengths measured, m , and three measurement vectors, N , C , and S , which are added in quadrature. Each of the vectors are quantified by the difference between a measured value, subscripted with G , and an expected value, subscripted with E . Note that these vectors can be quantified as shown in Equations 15, 16, and 17, which relate them back to parameters shown in Equation 12. A very accurate model will generally have an

$$N = \cos(2\Psi) \quad (15)$$

$$C = \sin(2\Psi) \cos(\Delta) \quad (16)$$

$$S = \sin(2\Psi) \sin(\Delta) \quad (17)$$

MSE less than 15 while a moderately accurate model will generally have an MSE in the range of 15 to 30. MSEs over 50 are a good indication that something in a given model is lacking.

It is worth mentioning here that global fitting SE models is a time consuming process that requires specific attention to even small changes in parameters with each pass. While it is a useful tool in estimating optical properties of a material, care must be taken when selecting which parameters to fix and which to float. If too many parameters are left to float, models can quickly lose their physical meaning even though the MSE may indicate a good fit. However, when certain parameter values cannot be assumed, allowing several values to float can be necessary for at least a first attempt. Subsequent passes can then be made for optimizing individual parameters. This was the general approach taken for the SE data used in this work.

To model n and k in the spectral range of 300 to 450 nm, which is often called the near UV, a different approach was required. This was necessary to account for the onset of absorption and the characteristic features it produces along the n and k profiles. Note that, unlike in the visible range, a value for k can no longer be assumed since the onset of absorption means it can neither be constant nor set to zero. For this section of the spectrum, a mathematical approach known as B-spline was used to construct n and k models. When choosing a B-spline model, the CompleteEASE software used for SE characterization allows flexibility in finding n and k arbitrarily over the range provided that a reasonable initial estimate is available. For this, the values for n at 632.8 nm (monochromatic red) found by the Cauchy model above were used. These values were 2.19 for CuI, 1.75 for Cu₂O, and 1.42 for PEDOT:PSS. After supplying these, an initial global fitting pass was performed which was then compared to UV-Vis absorbance results to evaluate if the results were a meaningfully accurate starting point. As both glass and

glass/ITO substrates are highly transparent, the issue of back reflection was also taken into consideration. Then, the first pass B-spline models were used to estimate thickness. This was compared to actual thicknesses measured by profilometry to make sure the models were fitting well to known values. To complete the models, n and k were parameterized for each material using a sum of oscillator functions. To optimize these oscillators, band gaps and other ellipsometry parameters from literature were used where the Cu-based materials were in thin film form.^{71, 72} It should be noted that these band gaps differed from those reported for bulk materials in Table 1. The amplitude and broadening parameters were then fitted as required. Finally, all parameters were optimized by only allowing one to vary at a time while holding the others fixed. The specifics of the initial oscillator parameters used for each Cu-based material model is shown in Table 2.

Table 2: B-spline modeling parameters for Cu-based HTLs deposited on glass/ITO substrates.

Material	Oscilators	Band Gap	Amplitude	Broadening
glass/ITO/CuI	1	2.9 eV	7.0	0.40
	2		9.1	0.51
	3		1.0	3.20
glass/ITO/Cu₂O	1	2.7 eV	10.0	1.80
	2		5.0	8.90
	3		-2.0	7.90

With SE models for each glass/ITO/HTL sample type completed, it was then time to plot the full n and k profiles. These plots can be seen in Figure 31 for each of the HTL materials as well as the substrate materials. To further confirm the validity of the models, they were also used to predict thicknesses of the components of the ITO/HTL bilayer. It should be noted that due to the high optical transparency of the HTL, ITO layer, and glass

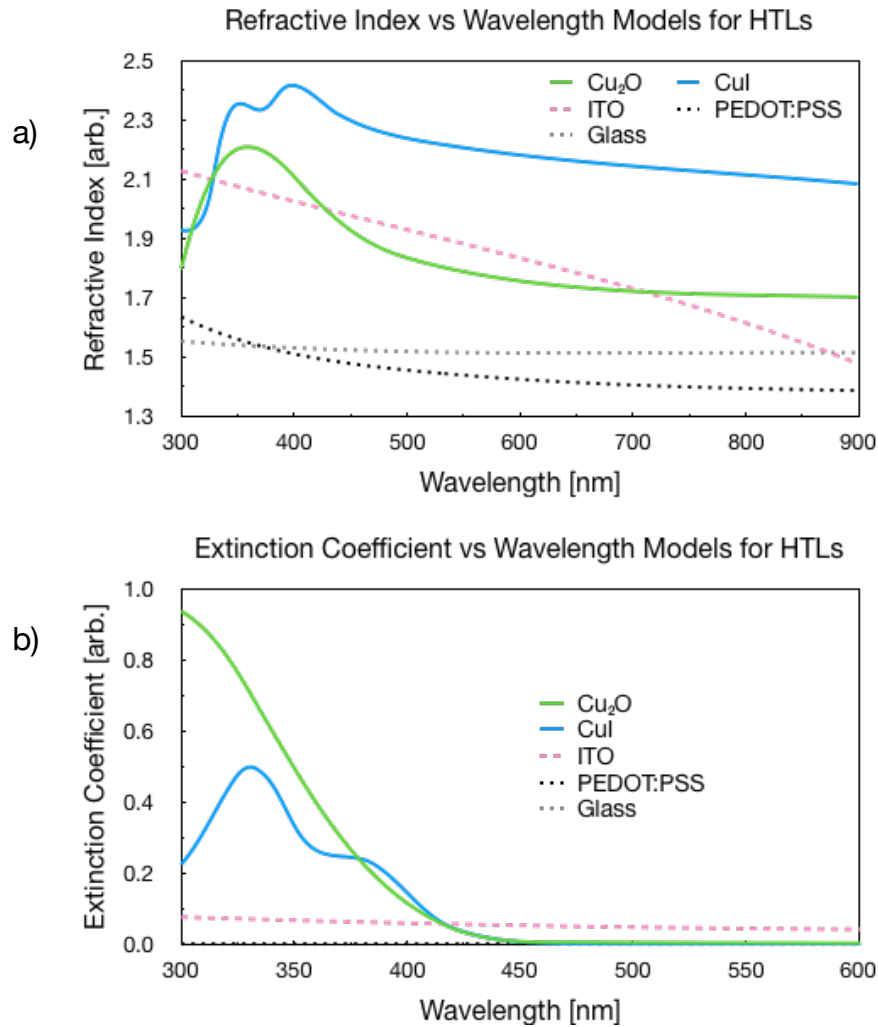


Figure 31: a) Refractive index, n , and b) extinction coefficient, k , profiles for the various HTLs and substrate materials modeled by CompleteEASE software.

substrate, it can be difficult for SE to differentiate between layer thicknesses since it measures light reflected off the interfaces. For this reason, a separate glass/ITO model was also constructed. When the full glass/ITO/HTL models were used to calculate thickness, AFM roughness measurements of the various HTLs were provided as a final fixed parameter to aid in fitting. Then, ITO and HTL thickness estimates were taken, allowing both values to float as well as fixing one value while allowing the other to float. These predicted thickness values can be seen in Table 3.

Table 3: Thickness predictions for ITO and HTL layers calculated from SE models with MSE values to show goodness of fit.

Sample	Parameters	Profilometer	Ellipsometry			
		HTL [nm]	HTL [nm]	ITO [nm]	Total [nm]	MSE [arb.]
CuI 30 mg/ml	ITO fixed HTL float	26.4	24.7	110.0	134.7	14.00
CuI 10 mg/ml		14.8	18.5	110.0	128.5	15.96
Cu ₂ O 30 mg/ml		12.9	16.0	110.0	126.0	30.36
Cu ₂ O 10 mg/ml		6.3	4.9	110.0	114.9	25.24
CuI 30 mg/ml	ITO float HTL float	26.4	25.4	109.4	134.8	15.92
CuI 10 mg/ml		14.8	19.0	108.7	127.7	15.75
Cu ₂ O 30 mg/ml		12.9	26.0	98.6	124.6	28.60
Cu ₂ O 10 mg/ml		6.3	19.9	97.9	117.8	14.93

When fixing the ITO thickness, the value was set at 110 nm, which was given by the manufacturer of the glass/ITO patterned substrates. For CuI samples, thickness values given by SE were in good agreement with profilometer data regardless of fixing the ITO thickness parameter. CuI HTLs made with 30 mg/ml and 10 mg/ml precursor solution concentrations had given SE thicknesses of 24.7 and 18.5 nm respectively when fixing the ITO thickness. The MSE for these calculations was given as 14.00 and 15.96 respectively. When allowing both thickness parameters to vary, CuI HTLs made with 30 mg/ml and 10 mg/ml precursor solution concentrations had given SE thicknesses of 25.4 and 19.0 nm respectively. The MSE for these calculations was given as 15.92 and 15.75 respectively. The ITO thickness for both of these calculations was approximately 109 nm, in good agreement with the known thickness.

For Cu₂O samples, thickness values given by SE were in good agreement with profilometer data only when fixing the ITO thickness parameter. Cu₂O HTLs made with

30 mg/ml and 10 mg/ml precursor solution concentrations had given SE thicknesses of 16.0 and 4.9 nm respectively when fixing the ITO thickness. The MSE for these calculations was given as 30.36 and 25.24 respectively. When allowing both thickness parameters to vary, Cu₂O HTLs made with 30 mg/ml and 10 mg/ml precursor solution concentrations had given SE thicknesses of 26.0 and 19.9 nm respectively. The MSE for these calculations was given as 28.60 and 14.93 respectively. The ITO thickness for both of these calculations was approximately 98 nm indicating they fit some parameters in error. This error is attributed to the optical similarity of the ITO and Cu₂O thin films. Despite this roughly 10 nm thickness error for each layer, the total ITO/HTL bilayer thicknesses were still in close agreement with the total thickness indicated by profilometry.

V. DEVICE ELECTRICAL CHARACTERIZATION

Champion Device J-V Characterization

While much of the analysis done in this work is concerned with characterizing the HTL, the real practical test for these materials is incorporating them into a working photovoltaic device. As the specifics of device J-V characterization were already given a thorough treatment in the introduction, this section will only cover the J-V results for the champion $\text{CH}_3\text{NH}_3\text{PbI}_3$ perovskite photovoltaic cells produced for this research. These results will include the J-V curves for the champion devices with CuI and Cu_2O HTLs as well as the associated PCE, FF, J_{SC} , and V_{OC} values.

Solar cell devices were characterized for device performance metrics by current-voltage analysis under AM1.5G simulated solar illumination. It should be noted that both forward and reverse J-V sweeps were taken at a constant rate of roughly 0.1 V/s. This revealed J-V hysteresis within most devices regardless of choice of HTL. For champion and other well-performing devices, this hysteresis was small, generally on the order of 0.5% PCE difference between forward and reverse sweeps. J-V hysteresis was a more noticeable issue when processing large batches of devices. Sample batches also showed statistically significant variations in performance metrics between devices. This will be discussed in more detail for each device architecture in the subsequent section on device population averages.

The J-V curve for the champion glass/ITO/CuI/ $\text{CH}_3\text{NH}_3\text{PbI}_3$ /C₆₀/BCP/Al device can be seen in Figure 32. Note that a small amount of hysteresis is visible between the forward and reverse sweeps, with the reverse sweep having a slightly higher PCE than

Champion CuI HTL Device JV Curve

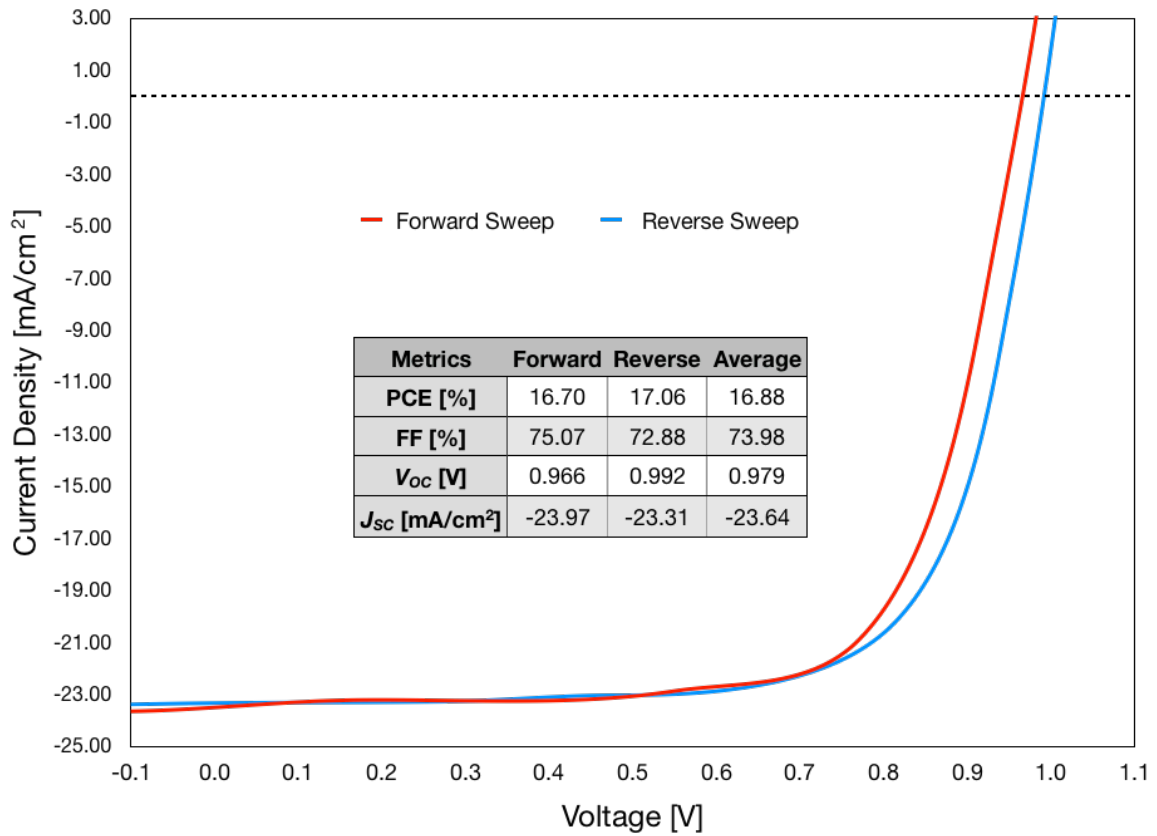


Figure 32: J-V curve for champion glass/ITO/CuI/CH₃NH₃PbI₃/C₆₀/BCP/Al device with inset performance values.

the forward sweep. The PCE for the forward and reverse sweeps is 16.70% and 17.06% respectively for a forward-reverse average of 16.88%. The reasonably high FF is clearly evidenced by the first part of the J-V curve appearing nearly flat with only a minute slope indicating a low shunting condition. The FF for the forward and reverse sweeps is 75.07% and 72.88% respectively for a forward-reverse average of 73.98%. The J_{sc} is nearly equal for both forward (at -23.57 mA/cm²) and reverse (at -23.31 mA/cm²) sweeps as the J-V hysteresis present is primarily acting along the voltage axis. V_{oc} values vary more widely between forward (at 0.966 V) and reverse (0.992 V) sweeps, with that difference producing much of the disparity in forward and reverse PCE values.

The J-V curve for the champion glass/ITO/Cu₂O/CH₃NH₃PbI₃/C₆₀/BCP/Al device can be seen in Figure 33. Note that the amount of hysteresis is less pronounced than that of the CuI HTL champion device. The hysteresis in this case stems from a difference in

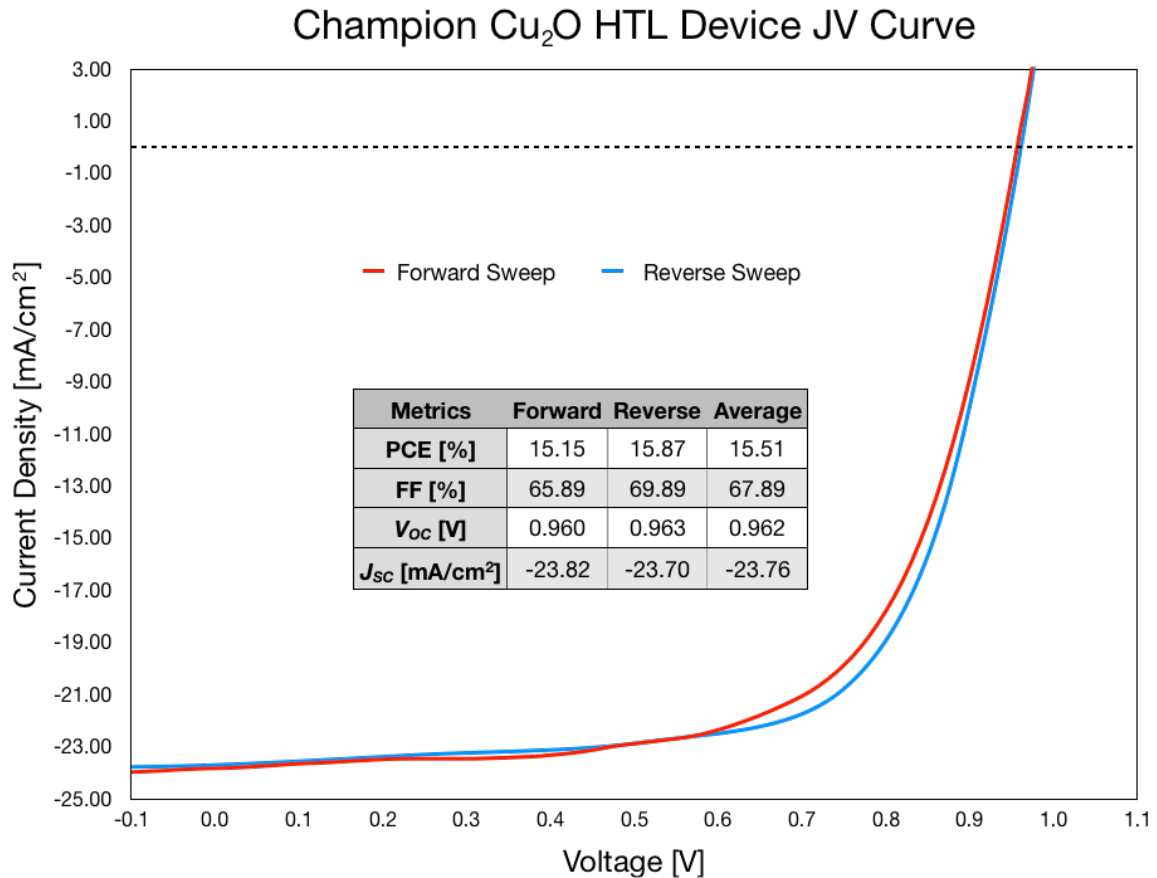


Figure 33: J-V curve for champion glass/ITO/Cu₂O/CH₃NH₃PbI₃/C₆₀/BCP/Al device with inset performance values.

ideality factor between forward and reverse sweeps as the J_{SC} and V_{OC} values are nearly equal for both sweeps. The PCE for the forward and reverse sweeps is 15.15% and 15.87% respectively for a forward-reverse average of 15.51%. The FF is lower for this device than the CuI HTL champion device with the culprit being a higher ideality factor overall as well as slightly more pronounced shunting. The FF for the forward and reverse sweeps is 65.89% and 69.89% respectively for a forward-reverse average of 67.89%. As mentioned, the J_{SC} values are nearly equal for both forward (at -23.82 mA/cm²) and

reverse (at -23.70 mA/cm^2) sweeps. The V_{OC} values are also nearly equal for forward (at 0.960 V) and reverse (0.963 V) sweeps.

Device Batch Averages and Deviations for Performance Metrics

The photovoltaic cell samples for this research were fabricated in batches of 16 devices evenly split over 4 glass/ITO patterned substrates. When fine tuning a process parameter for the first time, it was not uncommon to produce devices with less than 10% PCE. However, once all process parameters were optimized, device batch averages and deviations for all performance metrics improved. Once these results stabilized, a sample population was taken for a batch of devices with CuI HTLs and for a batch of devices

Table 4: Device performance metrics averages and deviations for solar cell sample populations with CuI and Cu_2O HTLs.

Device Performance Metrics	CuI HTL Average	CuI HTL Deviation	Cu_2O HTL Average	Cu_2O HTL Deviation
PCE Forward	14.59%	1.34%	12.34%	2.02%
PCE Reverse	15.72%	1.19%	13.17%	1.85%
PCE F/R Average	15.16%	1.25%	12.76%	1.86%
FF Forward	65.56%	4.39%	62.35%	5.15%
FF Reverse	67.69%	4.11%	65.25%	3.20%
FF F/R Average	66.62%	4.19%	63.80%	3.94%
V_{OC} Forward [V]	0.95	0.04	0.88	0.09
V_{OC} Reverse [V]	0.99	0.01	0.91	0.06
V_{OC} F/R Average [V]	0.97	0.02	0.90	0.07
J_{SC} Forward [mA/cm^2]	-23.47	0.67	-22.35	1.18
J_{SC} Reverse [mA/cm^2]	-23.38	0.67	-22.13	1.66
J_{SC} F/R Average [mA/cm^2]	-23.43	0.67	-22.24	1.37

with Cu₂O HTLs. All devices were made with optimized process parameters. The J-V results from these populations were used to calculate the PCE, FF, V_{OC} , and J_{SC} values seen in Table 4. Note that these include results for forward and reverse sweeps as well as a forward-reverse sweep average.

Due to flaws accidentally introduced through the standard device fabrication process, some devices would short or otherwise fail such that they produced no power output. Spin coating defects, particulate contamination, or shorting due to inaccurate Ag paint application were the primary culprits of a failed device. Such devices were easily linked to a likely failure mechanism and were not counted in sample populations. For the CuI HTL sample group, 12 of 16 devices were counted in the sample population. For the Cu₂O HTL sample group, 13 of 16 devices were counted in the sample population.

For both sample groups, the reverse sweep usually produced more power than the forward sweep due to a non-negligible amount of J-V hysteresis. This hysteresis was generally most visible along the voltage axis. Devices with a Cu₂O HTL commonly had a more pronounced hysteresis profile than those with a CuI HTL. Charge trapping at the HTL/perovskite interface is therefore a possible contributor to this hysteresis, considering the roughness and thickness of the Cu₂O HTLs produced for this work. Devices with a CuI HTL were far more consistent in producing J-V curves with a smaller amount of hysteresis.

When comparing PCE values, devices with a CuI HTL exhibited both a higher average PCE and lower deviation than their Cu₂O HTL counterpart. The PCE for the CuI HTL sample group was $15.16 \pm 1.25\%$ with a FF of $66.62 \pm 4.19\%$. The FF commonly

approached 70% and had nearly zero slope before the exponential bend of the J-V curve, indicating a very low shunting defect density.

Devices with a Cu₂O HTL had a lower average PCE of $12.76 \pm 1.86\%$. The larger deviation was likely related to the more pronounced hysteresis observed for this sample group. The FF for this sample group was also lower at $63.90 \pm 3.94\%$ due to a more noticeable slope from shunting as well as having a visibly higher ideality factor. The higher deviation in V_{OC} also appears to be a culprit in reducing PCE.

V_{OC} values were around 0.1 V higher for devices with a CuI HTL than those for devices with a Cu₂O HTL. The highest observed V_{OC} was 1.02 V for a CuI HTL device, although it was not the champion device. The average of 0.97 ± 0.02 V for this sample group shows how consistent V_{OC} was in such devices. Considering the average J_{SC} for this sample group, which was approximately -23.43 ± 0.67 mA/cm², it is conceivable that devices with this architecture could achieve a PCE of 18% or higher if a V_{OC} of 1.02 V could be reliably reproduced.

For devices with a Cu₂O HTL, V_{OC} ranged from as low as 0.75 V to as high as 0.97 V. The average and deviation of 0.90 ± 0.07 V for this sample group is a further indication of the performance disparity between devices with this architecture. J_{SC} values for this sample group, at an average of approximately -22.24 ± 1.37 mA/cm², were nearly on par with those of the CuI HTL sample group but also with a wider deviation. The larger inconsistency in this and other performance metrics for Cu₂O HTL devices is thought to arise from the amorphous morphology of the copper oxide thin films produced for this research.

J-V Modeling for Finding Resistances and Ideality Factor

PCE, FF, J_{SC} , and V_{OC} are device metrics that can be evaluated directly by measuring a solar cell's J-V curve. However, while these standard performance metrics can be reliably obtained from measurement alone, other device metrics, such as r_s , r_{sh} , and A , generally cannot. This is because contributions to resistivity and ideality factor within a device arise from phenomena internal to the materials that make up the device and its interfaces. In this work, r_{sh} , r_s , and A were calculated by fitting linear regressions to appropriate regions of J-V curves measured from solar cell samples. Two different linear regressions were employed, one on either side of the exponential bend of the J-V profile.

The first linear regression was used to calculate values for r_{sh} and J_L . Since shunt resistance behaves like a resistor added in parallel to a solar cell circuit, the J-V curve near J_{SC} can be treated as following an ohmic relationship. Thus, this region of J-V measurements can be fitted with a linear regression that obeys the relationship shown in Equation 7a when the diode current is effectively zero. This ohmic approximation is shown in Equation 18. The slope of this linear regression is therefore the reciprocal of

$$J(V) = \frac{V}{r_{sh}} - J_L \quad (18)$$

r_{sh} while the vertical intercept is J_L , which should be very nearly equal to J_{SC} . This allows the fitted value for r_{sh} to be further validated by confirming J_L with measured J_{SC} values.

The second linear regression was used to calculate values for r_s and A . Since series resistance behaves like a resistor added in series to a solar cell circuit, the resulting

J-V relationship obeys that shown in Equation 7b. Although this equation cannot be solved explicitly for $J(V)$, a linear relationship can be extracted from it by making a reasonable assumption about fabricated devices and applying some basic mathematical techniques. Starting with Equation 7b, assuming that r_{sh} is sufficiently large enough to neglect the shunting current term (which is generally reasonable for $r_{sh} \geq 0.5 \text{ k}\Omega\cdot\text{cm}^2$) allows a solution for the voltage bias in terms of total current, $V(J)$. Then, after taking a derivative of this function with respect to current, the result is a linear function of the differential resistivity, dV/dJ , with respect to the reciprocal of total current. This relationship is shown in Equation 19. It is necessary to point out that this function is only

$$\frac{dV}{dJ} = A \left(\frac{kT}{q} \right) (J_L + J_0 + J)^{-1} + r_s \quad (19)$$

approximately linear along the J-V curve from the exponential bend to the point of V_{OC} . Thus, this region of J-V measurements can be fitted with a linear regression that will

Table 5: Device J-V curve metrics averages and deviations for solar cell sample populations with CuI and Cu₂O HTLs.

Device J-V Curve Metrics	CuI HTL Average	CuI HTL Deviation	Cu ₂ O HTL Average	Cu ₂ O HTL Deviation
r_{sh} Forward [$\text{k}\Omega\cdot\text{cm}^2$]	0.959	0.358	0.547	0.369
r_{sh} Reverse [$\text{k}\Omega\cdot\text{cm}^2$]	0.997	0.250	0.612	0.565
r_{sh} F/R Average [$\text{k}\Omega\cdot\text{cm}^2$]	0.978	0.257	0.579	0.368
r_s Forward [$\Omega\cdot\text{cm}^2$]	4.0	1.9	2.3	0.7
r_s Reverse [$\Omega\cdot\text{cm}^2$]	1.9	1.3	2.2	0.7
r_s F/R Average [$\Omega\cdot\text{cm}^2$]	3.0	1.6	2.3	0.5
A Forward [arb.]	3.49	0.45	3.65	0.79
A Reverse [arb.]	3.82	0.57	3.14	0.61
A F/R Average [arb.]	3.66	0.48	3.39	0.63

yield A from the slope divided by kT/q and yield r_s directly from the vertical intercept.

r_s , r_{sh} , and A values were calculated for champion devices as well as for all samples in the CuI HTL and Cu₂O HTL device populations. This allowed for averages and deviations to be calculated for each of these metrics. These values are shown in Table 5. Note that these include results for forward and reverse sweeps as well as a forward-reverse sweep average. J-V curve models of the champion devices were then constructed with Equation 7a using measured values of V_{OC} (to calculate J_0) and fitted values of A , J_L , and r_{sh} . Also, with average and deviation values for all photovoltaic current parameters now available, J-V curve deviation ranges for each device type could be plotted. Fitted values of r_s were found to be sufficiently low enough to confidently exclude that

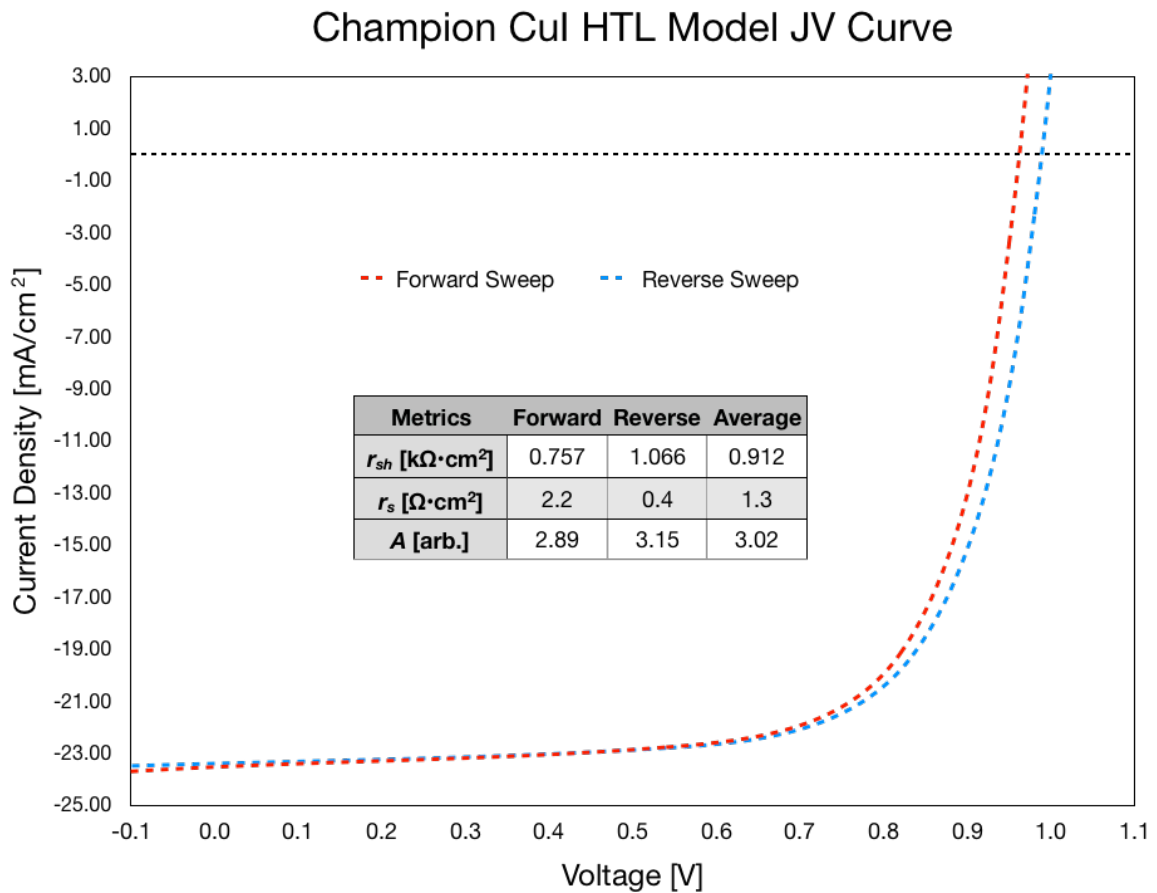


Figure 34: J-V model for champion glass/ITO/CuI/CH₃NH₃PbI₃/C₆₀/BCP/Al device with inset fitted resistivity and ideality factor values.

parameter from J-V curve modeling.

The J-V model for the champion glass/ITO/CuI/CH₃NH₃PbI₃/C₆₀/BCP/Al device can be seen in Figure 34. The ideality factor for the forward and reverse sweeps is 2.89 and 3.15 respectively for a forward-reverse average of 3.02. Shunt resistivity was calculated to be 0.757 and 1.066 kΩ•cm² for forward and reverse sweeps respectively for a forward-reverse average of 0.912 kΩ•cm². Series resistivity was very low with a forward-reverse average of 1.3 Ω•cm². This was a good indication that excluding series resistance from the J-V model curves was a reasonable approximation.

The J-V model for the champion glass/ITO/Cu₂O/CH₃NH₃PbI₃/C₆₀/BCP/Al device can be seen in Figure 35. The ideality factor for for this model varied more widely,

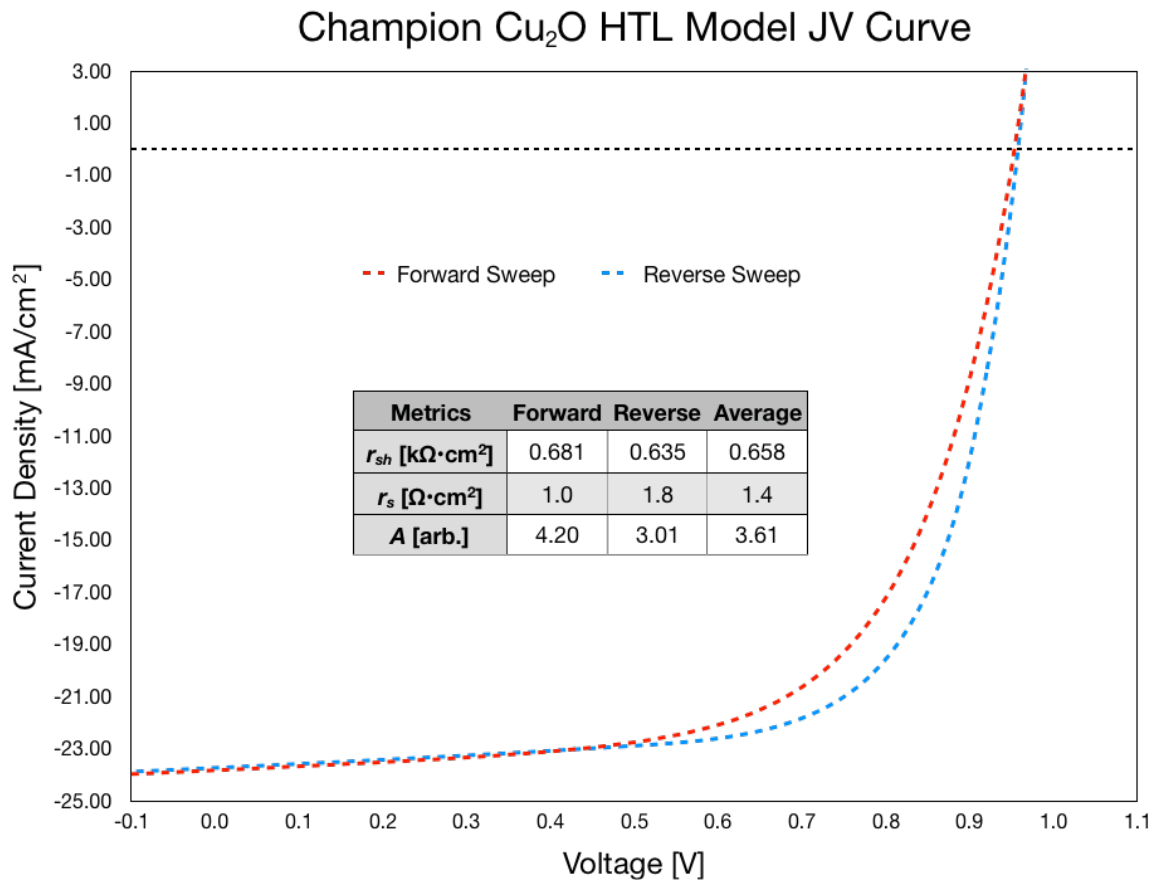


Figure 35: J-V model for champion glass/ITO/Cu₂O/CH₃NH₃PbI₃/C₆₀/BCP/Al device with inset fitted resistivity and ideality factor values.

with a forward and reverse sweep values of 4.20 and 3.01 respectively for a forward-reverse average of 3.61. This confirms that a difference in ideality factor is the origin of J-V hysteresis in the champion Cu₂O HTL device. Shunt resistivity was calculated to be lower in this device than the CuI HTL device but with less variation, with forward and reverse sweep values of 0.681 and 0.635 kΩ•cm² respectively for a forward-reverse average of 0.658 kΩ•cm². Series resistivity was again calculated to be around 1 Ω•cm².

Using the average and deviation values for all J-V curve parameters found in Tables 4 and 5, J-V curve ranges were plotted for both CuI HTL and Cu₂O HTL device populations. These can be seen in Figures 36 and 37 respectively. Note the obvious difference in deviation range between device types. CuI HTL devices were generally

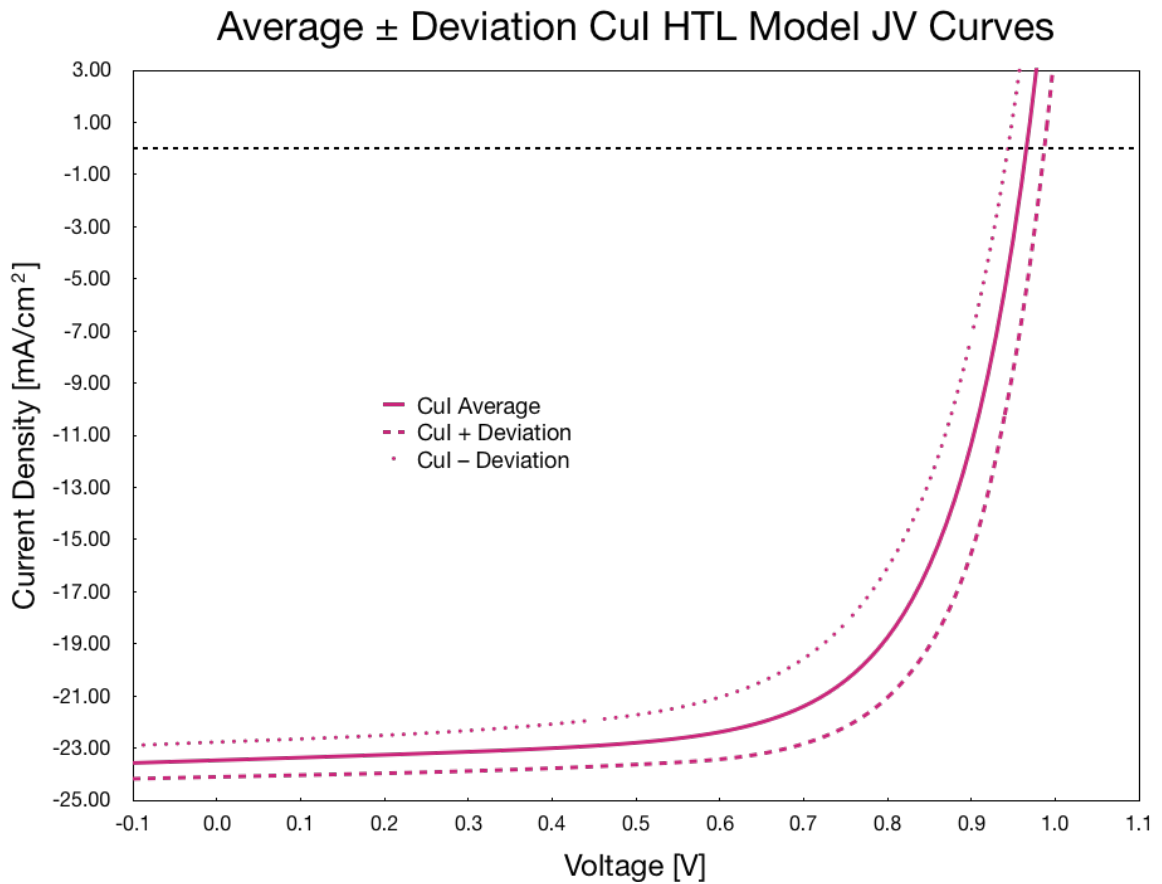


Figure 36: J-V curve deviation for glass/ITO/CuI/CH₃NH₃PbI₃/C₆₀/BCP/Al device population average.

superior in PCE and FF with a much smaller deviation over the population while the Cu₂O HTL device population varied more widely between performance parameter extrema.

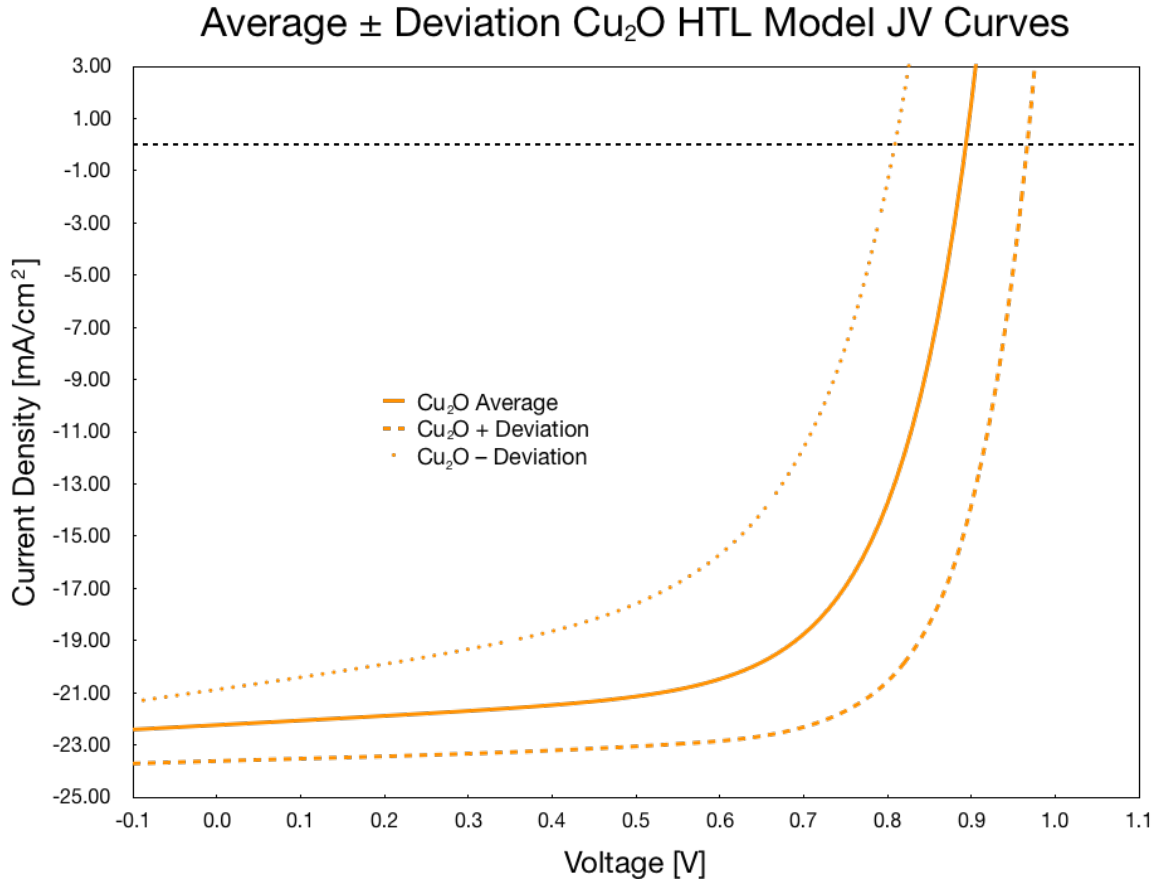


Figure 37: J-V curve deviation for glass/ITO/Cu₂O/CH₃NH₃PbI₃/C₆₀/BCP/Al device population average.

It is now necessary to mention that calculated r_{sh} and r_s values fell within the expected limits for the quality and type of solar cells produced in this study. The same is not true, however, for the calculated values of A , which exceeded the range of physical plausibility for all tested devices. Such a consistent error is a clear indication that the chosen J-V curve model cannot accurately account for the physical processes that determine ideality factor.⁷³ This shortcoming will thus require specific treatment in the conclusion and discussion section of this work regarding device J-V characterization.

VI. CONCLUSIONS

Properties of Copper Iodide and Copper Oxide HTLs

In this research CuI and Cu₂O thin films were investigated as potential HTL materials in inverted planar heterojunction organic perovskite photovoltaic cells. HTL thin films were deposited using simple solution chemistry and minimal thermal processing. HTL process parameters were carefully optimized, specifically controlling precursor solution concentration and spin coating deposition RPMs, until the highest quality HTLs were produced. HTL samples were characterized to determine their various physical properties. CuI thin films were found to be highly crystalline while copper oxide thin films were found to be amorphous.

AFM and SEM images revealed that CuI thin films had a clear grain structure with tightly packed grains ranging from 100 to 300 nm across. All copper oxide thin films were found to have a random and roughly textured surface regardless of annealing time and temperature. AFM roughness results matched the expected range for CuI samples, but was very high compared to layer thickness for copper oxide samples. These measurements seemed to indicate that all copper oxide thin films were amorphous. Additionally, EDS characterization indicated that all copper oxide thin films had roughly the same atomic ratios that were closer in composition to CuO than Cu₂O.

Profilometry measurements were used to determine HTL thicknesses. CuI thin films were 26.4 ± 2.5 nm thick on average when made with optimized process parameters. Cu₂O thin films were 12.9 ± 1.9 nm thick on average when made with optimized process parameters. After annealing, CuO thin films were generally less than

10 nm thick.

UV-Vis results showed that all HTL types had good optical transmission, generally 80% or more, in the range of 450 to 900 nm. Clear transmittance creases at 410 and 350 nm for CuI HTLs indicated a well-ordered γ -phase crystallinity. Absorbance data indicated an approximate band gap of 2.93 eV, which is close to the expected value from literature. The easily discernible absorption peak at 410 nm is likely due to the γ -CuI exciton binding energy of approximately 58 meV, which is more than double kT at room-temperature. A lack of transmittance creases and absorption peaks for all copper oxide films complicated band gap approximations, giving estimates that were significantly different from expected bulk material values.

XRD analysis confirmed crystal structure via Bragg 2θ diffraction measurements. CuI HTL samples had clear XRD peaks for the (111), (222), and (333) planes of single phase γ -CuI that forms in the zinc blende structure. Copper oxide HTL measurements showed only noise, definitively proving an amorphous morphology.

SE models for refractive index and extinction coefficient were constructed from various measurements and mathematical techniques. These gave HTL thickness results in reasonably close agreement with profilometer measurements. Furthermore, these models found more accurate band gap values for copper oxide thin films of 2.7 eV which was close to the approximate values found from UV-Vis absorbance data.

Efficacy of Cu-based HTLs in Organic Perovskite Solar Cells

The Cu-based HTLs were implemented in inverted planar heterojunction organic

perovskite photovoltaic cells with a glass/ITO/HTL/CH₃NH₃PbI₃/C₆₀/BCP/Al architecture. Both types of HTL researched produced working devices with appreciable device performance metrics. Devices with a CuI HTL were found to outperform devices with a Cu₂O HTL. The champion device with a CuI HTL had an average PCE of 16.88% with a FF of 73.98%, a V_{OC} of 0.98 V, and a J_{SC} of -23.44 mA/cm². The champion device with a Cu₂O HTL had an average PCE of 15.51% with a FF of 67.89%, a V_{OC} of 0.96 V, and a J_{SC} of -23.76 mA/cm².

Device J-V curves were also fitted with appropriate linear regressions to calculate values for r_{sh} , r_s , and A . J-V curve models were then constructed for the champion devices using a photovoltaic current equation that neglected series resistance. The champion device with a CuI HTL had an average ideality factor of 3.02 with a r_{sh} of 0.912 k Ω •cm² and a r_s of 1.3 Ω •cm². The champion device with a Cu₂O HTL had an average ideality factor of 3.61 with a r_{sh} of 0.658 k Ω •cm² and a r_s of 1.4 Ω •cm².

Performance results for the above champion devices were superior to literature reported devices with a PEDOT:PSS HTL but otherwise identical architecture.³⁶ Additionally, Cu-based HTLs were found to be stable in both atmosphere and controlled N₂ glovebox environments for up to three weeks without degrading. No significant performance differences were observed between devices made with stored HTLs versus new HTLs. This allowed for glass/ITO/HTL samples to be prepared well in advance of the rest of the device, easing processing logistics. Exposed PEDOT:PSS HTLs, however, were found to no longer be viable after only a few hours in normal atmosphere. These

results showed a clear advantage to using Cu-based inorganic HTLs over the organic polymer PEDOT:PSS in methylammonium lead iodide based perovskite solar cells.

Consequences of Single Parameter Modeling of Ideality Factor

The photovoltaic current model chosen for this study, shown in Equations 7a and b, assumes a single junction $p-n$ photodiode device requiring single parameters for J_0 , J_L , r_{sh} , r_s , and A . While this model gave physically meaningful results for J_0 , J_L , r_{sh} , and r_s , the calculated values for A , which were generally 3 or greater, were in excess of the theoretically understood range. It is therefore reasonable to conclude that the presented approach to modeling J-V characteristics in organic perovskite solar cells is problematic when attempting to account for the effects of recombination within the device. Interestingly, despite this issue, the ideality factor values reported in this work are in close agreement with those found in literature for a similar device architecture.⁷⁴

A useful way to understand the physical significance of the ideality factor is to consider it as the average number of carriers participating in the recombination process. Conceptually, this restricts the value of A to positive integers from 1 to 3, each representing a particular recombination mechanism. These can be seen in Table 6. Notice

Table 6: Recombination mechanisms and associated ideality factor values.⁷⁵

Recombination Mechanism	Ideality Factor	Carrier Description
Band-to-band (Shockley-Read-Hall)	1	Minority carriers only (low injection)
Band-to-band (Shockley-Read-Hall)	2	Minority and majority carriers (high injection)
Depletion Region	2	Electron and hole recombination at junction
Auger Effect	3	Two majority and one minority carriers

that Auger recombination is the only mechanism that gives an ideality factor equal to 3. However, as Auger recombination only occurs under high-energy scenarios, it is almost assuredly not occurring in solar cells operating under standard solar illumination. This leaves only low level and high level injection circumstances as possible recombination processes in solar cell devices.

Recall that in the original Diode Law the contributions to total current are only diffusion and minority carrier recombination. These low injection conditions give a theoretical ideality factor of exactly 1. Under high injection conditions, as is the case in a photovoltaic cell, total current also includes photogeneration and recombination in the depletion region, which gives a theoretical ideality factor of up to 2. In order for the ideality factor of a device to exceed 2, recombination and additional transport effects in other layers and interfaces must be present. As such, an adjusted photovoltaic current model that includes multiple junctions is worth a brief discussion here.

The photovoltaic devices produced for this research consisted of six independent layers. As a result, there are potentially five interfaces that could each be treated as a *p-n* junction diode, each contributing their own current, voltage, resistance, and ideality factor parameters. While a five junction representation is likely to be unnecessarily overcomplicated, a two junction model, one for each transport/intrinsic layer interface, is a logical revision to the single junction standard. This new approach, known as the heterojunction diffusion model, is shown in Equation 20.⁷³ It contains two diode current

$$J = J_D(e^{q(V-Jr_s)/A_DkT} - 1) + J_R(e^{q(V-Jr_s)/A_RkT} - 1) - J_L + \frac{V - Jr_s}{r_{sh}} \quad (20)$$

terms, one for diffusion current, J_D , and one for recombination current, J_R , each with their own ideality factors, A_D and A_R respectively. Although the total ideality factor for the device cannot be simply obtained by adding A_D and A_R , both will contribute to the curvature of the characteristic J-V curve exponential bend.

A final note should be made that J-V curve fitting using the linear regressions presented in Equations 18 and 19 is no longer sufficient to calculate values for A_D and A_R . Furthermore, as there is now more than one junction in this model, simple assumptions about r_{sh} and r_s across the full device are no longer justified. As a result, Equation 20 can no longer be solved explicitly for J in terms of V . Thus, numerical methods beyond the scope of this research will be required to appropriately fit J-V curves to this model. This exercise is left as a recommendation for future work regarding these devices.

Considerations for Further Research

It should be briefly noted that there were a few items lacking exposure in this research that deserve attention in future work regarding the HTLs studied here. While carrier mobilities were specifically referenced from literature, they were not measured as a part of this study. The quality of the CuI and Cu_xO thin films could be further evaluated if experimentally measured mobilities were taken. Also, due to the availability of HTL materials, PEDOT:PSS was the only organic polymer HTL compared to the Cu-based HTLs utilized in this work. There are many more organic polymers currently under scrutiny that also deserve comparison, including PTAA, which has recently attracted attention due to record V_{OC} values.

When considering J-V characterization and curve modeling, the observed ideality factor values deviated from photovoltaic device theory, indicating that a more detailed model should be employed. The heterojunction diffusion model is recommended, with ideality factor parameters fitted by fixing one at a time to theoretical values, allowing the other parameter to float. Further junctions could also be included if the two diode extension proves insufficient. This would require mathematical methods and tools beyond those presented in this work. Additionally, the effects of temperature on ideality factor could also be explored as thermal effects are important to charge carrier transport.

Other device components also deserve more attention than treated here as no optimization was done for any layer other than the HTL. In particular, the ETL and/or buffer layer could be optimized, either by changing thicknesses, or by trying other known ETL materials such as PCBM. Finally, a focus on perovskite degradation when using inorganic Cu-based HTLs is also a welcome research topic considering the well-known effects of organic polymer transport layers on device longevity.

APPENDIX SECTION

The purpose of this appendix is to provide supplementary information regarding equipment and measurement specifications for the characterization methods used in this research. This material is intended to give the necessary details required to reproduce the reported methodology and results. Each analysis tool will now be treated in the same order as they appeared previously.

Atomic Force Microscopy

The AFM equipment model was the Bruker Dimension ICON. The measurement mode used for all samples was the “tapping mode” performed in normal atmosphere. The AFM tip type used was HQ:NSC14/AL BS. This tip has an average operating frequency of 160 kHz with an average force constant of 5 N/m. The cantilever amplitude was set between 8 and 15 nm depending on the vertical resolution required by a sample.

Stylus Profilometry

The stylus profilometer equipment model was the Bruker DektakXT. The stylus tip radius was 2 μm . The stylus tip force was 3 mg. The scan length for all measurements was 500 nm.

Scanning Electron Microscopy and Energy Dispersive X-Ray Spectroscopy

The SEM equipment model was the FEI Helios NanoLab 400 DualBeam. The lens configuration was a semi in-lens objective with a through-the-lens detector. The

accelerating voltage and beam current were the same for both SEM and EDS measurements for a given sample type. For glass/ITO/CuI samples, the accelerating voltage and beam current were 10 kV and 0.34 nA respectively. For glass/ITO/Cu_xO samples, the accelerating voltage and beam current were 10 kV and 86 pA respectively. For the device cross-section image, the accelerating voltage and beam current were 8 kV and 43 pA respectively. The FIB used to cut the cross-section was a cobalt source with an accelerating voltage of 10 kV for the initial ion milling and 0.5 kV for clean up.

Ultraviolet-Visible Spectroscopy

The UV-Vis equipment model was the Shimadzu UV-2501PC. Transmittance, absorbance, and reflectance measurement modes were supported. The maximum wavelength range permitted by the tool was 190 to 1100 nm with a resolution of 0.1 nm. Sample measurements in this work used only the 200 to 900 nm range. The beam was 12 mm tall and 2 mm wide.

X-Ray Diffraction Crystallography

The XRD equipment model was the Rigaku SmartLab X-Ray Diffractometer. The measurement mode used for all samples was the Bragg-Brentano $2\theta/\theta$ continuous scan. The voltage and current for the x-ray source was 40 kV and 44 mA respectively. The x-ray wavelength was approximately 1.5 nm. The source-side length-limiting slit was 5 mm wide. The detector-side monochromator was the 5.0° Soller slit. The sample stage was the 0–3 mm spacer with a 4-inch wafer sample plate. All scans were done from 20° to 90°.

Spectroscopic Ellipsometry

The SE equipment model was the J.A. Woollam Co. M-2000UI with an Auto Angle ESM-300 Base. The detector type was a CCD. The maximum wavelength range permitted by the tool was 245 to 1690 nm with a resolution of 660 wavelengths per measurement. Sample measurements in this work used only the 200 to 900 nm range. Each measurement was performed at 45°, 55°, 65°, and 75° angles of incident. The analysis software was CompleteEase provided by the J.A. Woollam Company.

Device J-V Characterization

The photovoltaic devices produced for this research were characterized by a solar simulator with an AM1.5G illumination. The J-V curves were measured using a Keithly 2400 SourceMeter multimeter device. A LabView (2014 version) virtual instrument specifically designed for this characterization was used to collect the digital data output by the solar simulator and multimeter apparatus. The virtual instrument then calculated J_{SC} , V_{OC} , FF, and PCE from the collected data. All J-V sweeps were done at a rate of approximately 0.1 V/s.

REFERENCES

1. Bacquerel, E. Mémoire sur les effets électriques produits sous l'influence des rayons solaires. *Comptes Rendus* **9**, 561–567 (1839).
2. Perlin, J. From Selenium to Silicon. *Let it Shine: The 6000 Year History of Solar Energy* (2013). <<http://john-perlin.com/let-it-shine.html>>
3. The Nobel Prize in Physics 1918. *Nobel Media AB* (2019).
4. The Nobel Prize in Physics 1921. *Nobel Media AB* (2019).
5. Riordian, M. & Hoddeson, L. The origins of the pn junction. *IEEE Spectrum* June, 46–51 (1997).
6. Chodos, A. Bell Labs Demonstrates the First Practical Silicon Solar Cell. *APS News* **18** (4) (2009). <<https://www.aps.org/publications/apsnews/200904/physicshistory.cfm>>
7. Schaub, J. Vanguard I - the World's Oldest Satellite Still in Orbit. *U.S. Navy Web Archives* (1999). <<https://web.archive.org/web/20150321054447/http://code8100.nrl.navy.mil/about/heritage/vanguard.htm>>
8. Carr, G. Sunny uplands: Alternative energy will no longer be alternative. *The Economist* November (2012). <<https://www.economist.com/news/2012/11/21/sunny-uplands>>
9. Noah, B. Who Owns the Sun?. *Bloomberg Newsweek* January 28 (2016). <<https://www.bloomberg.com/features/2016-solar-power-buffett-vs-musk/>>
10. Swanson, R. M. A vision for crystalline silicon photovoltaics. *Progress in Photovoltaics: Research and Applications* **14** (5), 443–453 (2006).
11. Green, M. The Path to 25% Silicon Solar Cell Efficiency: History of Silicon Cell Evolution. *Progress in Photovoltaics: Research and Applications* **17**, 183–189 (2009).
12. Solar Panels Cost. *Solar Power For Us* September 21 (2016). <<https://www.solarenergyforum.com/solar-panels-cost/>>
13. Tooley, M. *Electronic Circuits: Fundamentals and Applications*. (Routledge, 2013).

14. Shockley, W. The Theory of *p-n* Junctions in Semiconductors and *p-n* Junction Transistors. *The Bell System Technical Journal* **28** (3), 435–489 (1949).
15. Sze, S. M. & Kwok, K. Ng. *Physics of Semiconductor Devices*. (Wiley-Interscience, 2003).
16. Böer, K. W. *Handbook of the Physics of Thin-Film Solar Cells*. (Springer, 2013).
17. Park, N. & Segawa, H. Research Direction toward Theoretical Efficiency in Perovskite Solar Cells. *ACS Photonics* **5**, 2970–2977 (2018).
18. Wenk, H. & Bulakh, A. *Minerals: Their Constitution and Origin*. (Cambridge University Press, 2004).
19. Levy, M. *Crystal Structure and Defect Properties in Ceramic Materials*. PhD dissertation, Imperial College London, Department of Materials (2005).
20. Travis, W. & Glover, E. *et al.* On the application of the tolerance factor to inorganic and hybrid halide perovskites: a revised system. *Chemical Science* **7**, 4548 (2016).
21. Li, Z. *et al.* Stabilizing Perovskite Structures by Tuning Tolerance Factor: Formation of Formamidinium and Cesium Lead Iodide Solid-State Alloys. *Chemistry of Materials* **28** (1), 284–292 (2016).
22. Moa, Y. *et al.* Synthesis, Properties, and Applications of Perovskite-Phase Metal Oxide Nanostructures. *Material Matters* **5.2**, 50 (2010).
23. Kojima, A. *et al.* Organometal Halide Perovskites as Visible-Light Sensitizers for Photovoltaic Cells. *Journal of the American Chemical Society* **131** (17), 6050–6051 (2009).
24. Chen, J. *et al.* Single-Junction Polymer Solar Cells Exceeding 10% Power Conversion Efficiency. *Advanced Materials* **27** (6), 1035–1041 (2014).
25. Best Research-Cell Efficiencies. *National Renewable Energy Laboratories* January 3 (2019). <<https://www.nrel.gov/pv/assets/pdfs/pv-efficiency-chart.20190103.pdf>>
26. Perovskite Solar. *Perovskite-info* January 8 (2018). <<https://www.perovskite-info.com/perovskite-solar>>
27. Sadler, J. A. *Optical Mapping of Organohalide Lead Perovskite Films*. MS thesis, Texas State University, Department of Physics (2018).

28. Saidi, A. & Choi, J. Nature of the cubic to tetragonal phase transition in methylammonium lead iodide perovskite. *The Journal of Chemical Physics* **145**, 144702 (2016).
29. Moustafa A. M. *et al.* Structural Characterization of Substituted Calcium Titanate Compounds $\text{Ca}_{1-x}\text{La}_x\text{Ti}_{1-x}\text{Fe}_x\text{O}_3$. *Egyptian Journal of Solids* **27** (2), 213–222 (2004)
30. Herz, L. M. Charge-Carrier Mobilities in Metal Halide Perovskites: Fundamental Mechanisms and Limits. *ACS Energy Letters* **2**, 1539–1548 (2017).
31. Xia, Y. *et al.* Management of perovskite intermediates for highly efficient inverted planar heterojunction perovskite solar cells. *Journal of Materials Chemistry A* **5**, 3193 (2017).
32. Rühle, S. Tabulated values of the Shockley–Queisser limit for single junction solar cells. *Solar Energy* **130**, 139–147 (2016).
33. Manspecker, C. *et al.* Role of interface in stability of perovskite solar cells. *Current Opinion in Chemical Engineering* **15**, 1–7 (2017).
34. Fakharuddin, A. *et al.* Interfaces in Perovskite Solar Cells. *Advanced Energy Materials* **7** (22), 1700623 (2017).
35. Zhang, W. *et al.* Interface engineering with NiO nanocrystals for highly efficient and stable planar perovskite solar cells. *Electrochimica Acta* **293**, 211–219 (2019).
36. Hasan, M. & Venkatesan, S. *et al.* Tailoring the Nucleation and Grain Growth by Precursor Phase Ratio for Efficient Organic Lead Halide Perovskite Optoelectronic Devices. *Journal of Materials Chemistry C* **5**, 10114–10121 (2017).
37. Liu, Z. *et al.* Open-Circuit Voltages Exceeding 1.26 V in Planar Methylammonium Lead Iodide Perovskite Solar Cells. *ACS Energy Letters* **4**, 110–117 (2018).
38. Malinkiewicz, O. Perovskite solar cells employing organic charge-transport layers. *Nature Photonics* **8** (2), 128–132 (2013).
39. Raship, N. A. *et al.* Effect of annealing temperature on the properties of copper oxide films prepared by dip coating technique. *AIP Conference Proceedings* **1788**, 030121 (2017).
40. de Jong, M. P. *et al.* Stability of the interface between indium-tin-oxide and poly(3,4-ethylenedioxythiophene)/poly(styrenesulfonate) in polymer light-emitting diodes. *Applied Physics Letters* **77**, 2255 (2000).

41. Bracher, C. *et al.* Degradation of inverted architecture $\text{CH}_3\text{NH}_3\text{PbI}_{3-x}\text{Cl}_x$ perovskite solar cells due to trapped moisture. *Energy Science & Engineering* **6** (1), 35–46 (2018).
42. Eames, C. *et al.* Ionic transport in hybrid lead iodide perovskite solar cells. *Nature Communications* **6**, 7497 (2015).
43. Hönerlage, B. CuI: lattice constants. *New Data and Updates for I-VII, III-V, III-VI and IV-VI Compounds*. (Springer, 2008).
44. Madelung, O. *et al.* Cuprous oxide (Cu_2O) crystal structure, lattice parameters. *Non-Tetrahedrally Bonded Elements and Binary Compounds I*. (Springer, 1998).
45. Madelung, O. *et al.* Cupric oxide (CuO) crystal structure, lattice parameters. *Non-Tetrahedrally Bonded Elements and Binary Compounds I*. (Springer, 1998).
46. Chen, D. *et al.* Growth Strategy and Physical Properties of the High Mobility P-Type CuI Crystal. *Crystal Growth & Design Communication* **10**, 2057–2060 (2010).
47. Meyer, B. K. *et al.* Binary copper oxide semiconductors: From materials towards devices. *Physica Status Solidi* **249** (8), 1487–1509 (2012).
48. Guo, Y. *et al.* Single phase, high hole mobility Cu_2O films as an efficient and robust hole transporting layer for organic solar cells. *Journal of Materials Chemistry A* **5**, 11055 (2017).
49. Zheng, W. *et al.* The Phase Evolution and Physical Properties of Binary Copper Oxide Thin Films Prepared by Reactive Magnetron Sputtering. *Materials* **11**, 1253 (2018).
50. Tsang, S.W. *et al.* PEDOT:PSS polymeric conducting anode for admittance spectroscopy. *Organic Electronics* **7**, 474–479 (2006).
51. Lenz, A. *et al.* The electronic structure and reflectivity of PEDOT:PSS from density functional theory. *Chemical Physics* **384**, 44–51 (2011).
52. Bruno, T. J. & Svoronos, P. D. N. *CRC Handbook of Fundamental Spectroscopic Correlation Charts*. (CRC Press, 2005).
53. Liu, A. *et al.* In situ one-step synthesis of p-type copper oxide for low-temperature, solution-processed thin-film transistors. *Journal of Materials Chemistry A* **5**, 2524 (2017).

54. Chen C. *et al.* Effect of BCP buffer layer on eliminating charge accumulation for high performance of inverted perovskite solar cells. *RCS Advances* **7**, 35819 (2017).
55. Binnig, G. *et al.* Atomic Force Microscope. *Physical Review Letters* **56** (9), 930–933 (1986).
56. Morrison, E. The development of a prototype high-speed stylus profilometer and its application to rapid 3D surface measurement. *Nanotechnology* **7**, 37–42 (1996).
57. García, J. C. *et al.* Some Considerations about the Use of Contact and Confocal Microscopy Methods in Surface Texture Measurement. *Materials* **11**, 1484 (2018).
58. Mohammed, A. & Abdullah, A. Scanning Electron Microscopy (SEM): A Review. *International Conference on Hydraulics and Pneumatics Proceedings* (2018).
59. Stokes, D. J. *Principles and Practice of Variable Pressure Environmental Scanning Electron Microscopy (VP-ESEM)*. (John Wiley & Sons, 2008).
60. Borrajo-Pelaez, R. & Hedström, P. Recent Developments of Crystallographic Analysis Methods in the Scanning Electron Microscope for Applications in Metallurgy. *Critical Reviews in Solid State and Materials Sciences* **43** (6), 455–474 (2018).
61. Goldstein, J. *et al.* *Scanning Electron Microscopy and X-Ray Microanalysis*. (Springer, 2003).
62. Perkampus, H-H. *UV-Vis Spectroscopy and Its Applications*. (Springer, 1992).
63. Amalina, M. N. *et al.* The properties of copper (i) iodide (CuI) thin films prepared by mister atomizer at different doping concentration. *Procedia Engineering* **56**, 731–736 (2013).
64. Zhou, K. *et al.* Highly efficient organic solar cells based on a robust room-temperature solution-processed copper iodide hole transporter. *Nano Energy* **16**, 458–469 (2015).
65. Sun, W. *et al.* Solution-Processed Copper Iodide as an Inexpensive and Effective Anode Buffer Layer for Polymer Solar Cells. *The Journal of Physical Chemistry C* **118**, 16806–16812 (2014).
66. Yang, C. *et al.* Room-temperature synthesized copper iodide thin film as degenerate *p*-type transparent conductor with a boosted figure of merit. *Proceedings of the National Academy of Sciences* **133** (46), 12929–12933 (2016).

67. Ahn, D. & Park, S. H. Cuprous halides semiconductors as a new means for highly efficient light-emitting diodes. *Nature Scientific Reports* **6**, 20718 (2016).
68. Mugwang'a, F. K. *et al.* Optical characterization of Copper Oxide thin films prepared by reactive dc magnetron sputtering for solar cell applications. *International Journal of Thin Film Science and Technology* **2** (1), 15–24 (2013).
69. Kittel, C. *Introduction to Solid State Physics*. (John Wiley & Sons, 2005).
70. Ellipsometry FAQ. *J. A. Woollam Ellipsometry Solutions* (2019). <<https://www.jawoollam.com/resources/ellipsometry-faq>>
71. Tompkins, H. & Irene, E. A. *Handbook of Ellipsometry*. (William Andrew, 2005).
72. Mohamed, S. A. *et al.* CuI as versatile hole-selective contact for organic solar cell based on anthracene-containing PPE–PPV. *Solar Energy Materials & Solar Cells* **143**, 369–374 (2015).
73. Liao, P. *et al.* A New Method for Fitting Current–Voltage Curves of Planar Heterojunction Perovskite Solar Cells. *Nano-Micro Letters* **10**, 5 (2018).
74. Wang, Y. K. *et al.* Vapour-assisted multi-functional perovskite thin films for solar cells and photodetectors. *Journal of Materials Chemistry C* **4** (31), 7415–7419 (2016).
75. Ideality Factor. *PV Education* (2014). <<https://www.pveducation.org/pvcdrom/solar-cell-operation/ideality-factor>>